CRITICAL BEHAVIOUR OF $CsMnBr_3$

By

THOMAS EDWARD MASON, B.Sc.

A Thesis

Submitted to the School of Graduate Studies

in Partial Fulfilment of the Requirements

for the Degree

Doctor of Philosophy

McMaster University

September 1990

CRITICAL BEHAVIOUR OF $CsMnBr_3$

Doctor of Philosophy (1990) McMaster University

(Physics) Hamilton, Ontario

TITLE: Critical Behaviour of $CsMnBr_3$

AUTHOR: Thomas Edward Mason, B.Sc. (Dalhousie University)

SUPERVISOR: Professor M.F. Collins

NUMBER OF PAGES: ix, 101

ABSTRACT

The critical behaviour of $CsMnBr_3$ has been studied by magnetic neutron scattering, magnetic susceptibility measurements, and Monte Carlo simulations. The magnetic Mn^{+2} ions in this insulating material form a simple hexagonal lattice. In the absence of an applied magnetic field the Mn^{+2} magnetic moments order in a 120° structure with the spins confined to the ab-plane.

Neutron scattering measurements of the temperature dependence of the paramagnetic critical scattering and the antiferromagnetic order parameter have found critical exponents $\gamma = 1.01 \pm 0.08$, $\upsilon = 0.54 \pm 0.03$, and $\beta = 0.21 \pm 0.02$. These exponents do not correspond to any of the standard universality classes. This is a consequence of the $Z_2 \times S_1$ symmetry of the order parameter arising from its XY (S_1) and chiral (Z_2) degeneracy.

Elastic neutron scattering has been used to determine the magnetic phase diagram of $CsMnBr_3$. The application of a magnetic field along the <100> direction splits the zero field transition and results in a intermediate phase (II) of spin-flop character. The zero field transition is a tetracritical point with cross-over exponents $\psi_{P\text{-}II} = 1.21 \pm 0.07$ and $\psi_{II\text{-}I} = 0.75 \pm 0.05$. The

fact that both exponents are less than two reflects the narrowness of the temperature range over which the intermediate phase is stable. These exponents are not in agreement with the theoretical prediction $\psi_{P\text{-}II} = \psi_{II\text{-}I} \cong 1.04$.

Magnetic susceptibility (χ) measurements near the tetracritical point have shown that the phase transition is marked by a discontinuous change in the slope of χ. This is in contrast to the predictions of scaling theory that there should be a singularity at T_N where χ goes to zero.

Monte Carlo simulations of $CsMnBr_3$ have been performed to determine to what extent the magnetic Hamiltonian is consistent with the observed phase diagram. The results reproduce the qualitative features of the phase diagram including the tetracriticality of the zero field transition and the increase of the Néel temperature with increasing magnetic field. A substantial renormalization of the Néel temperature with the size of the lattice along the c direction due to the quasi-one-dimensional nature of the system is observed. This is consistent with a strong suppression of the Néel temperature when the system is diluted with non-magnetic impurities.

ACKNOWLEDGEMENTS

I am pleased to thank my supervisor Dr. M.F. Collins for his guidance and instruction and for giving me the opportunity to work on many interesting magnetic systems. Much of the work covered in this thesis also involved collaboration with Dr. B.D. Gaulin to whom I express my gratitude. During my time a Chalk River I benefitted greatly from the experience of the members of the Neutron and Solid State Physics group, particular thanks go to Dr. W.J.L. Buyers for his instuction and also his hospitality. During my tenure as a graduate student I have been fortunate enough to work in collaboration with various researchers and other students all of whom have contributed to my understanding of physics and neutron scattering. Finally I thank Jennifer for putting up with my absences while I was doing experiments.

TABLE OF CONTENTS

LIST OF FIGURES

CHAPTER 1

INTRODUCTION

1.1 General Outline

The study of phase transitions in magnetic systems is of interest both because of the technological importance of many magnetic materials and because of the more fundamental questions about the statistical mechanics of cooperative phenomena. Although phase transitions are not unique to magnetic systems much of the current understanding of the physics of phase transitions has come from studies of magnetism due, in part, to the relative simplicity of the appropriate Hamiltonians. This is particularly true in the case of critical phase transitions where the universality hypothesis (Kadanoff 1971) states that the behaviour of systems near critical points fall into classes defined according to simple physical criteria. Consequently results obtained for magnetic systems can be applied to any critical phase transition in the same universality class.

This thesis deals with studies of the critical behaviour of the insulating antiferromagnet $CsMnBr_3$ by neutron scattering and Monte Carlo computer simulations. Although the work deals with the properties of a particular material it has more general implications arising from its

relevence to the question of what physical criteria define the various universality classes.

The remainder of this chapter is devoted to a discussion of the general features of critical phase transitions and model magnetic systems. It concludes with a survey of the structural and magnetic properties of $CsMnBr_3$. Chapter 2 is a review of neutron scattering as it applies to the study of magnetic phase transitions. The measurement of the critical exponents for $CsMnBr_3$ in the absence of an applied magnetic field is described in Chapter 3. The determination of the magnetic phase diagram is covered in Chapter 4 along with measurements of the magnetic susceptibility. Chapter 5 presents the results of numerical simulations of the magnetic Hamiltonian of $CsMnBr_3$. Concluding remarks are made in Chapter 6.

The work covered in this thesis has been published in the scientific literature (Mason et al 1987, Gaulin et al 1989a, Mason et al 1989, Gaulin et al 1989b, Mason et al 1990a, and Mason et al 1990b). Additional work not covered in this thesis includes neutron scattering studies of the heavy fermion superconductor URu_2Si_2 (Mason et al 1990c and Broholm et al 1990), the Kondo lattice compound $CePd_2Si_2$ (Steeman et al 1990), and the high temperature superconductor $YBa_2Cu_3O_{6+x}$ (Tranquada et al 1990) as well as Monte Carlo simulations of percolation in a two dimensional triangular antiferromagnet (Harrison and Mason 1990).

1.2 Critical Phase Transitions

Phase transitions between different states are a feature found in systems with many interacting components. The boiling of water is the transition from the liquid to the gaseous state which occurs over a range of well defined temperatures and pressures. This is an example of a first order transition because the first derivative of the appropriate thermodynamic potential (the Gibbs free energy, G) is discontinuous at the phase transition. The latent heat observed for such a transition is a consequence of this. There are many phase transitions in which there is no discontinuity in the first derivative of G, these cases are referred to as critical phase transitions and they are usually signalled by non-analytic behaviour of G. Because of the absence of a discontinuity in the first derivative of G there is no latent heat associated with a critical phase transition. Critical phase transitons are found in magnetism, superconductivity, superfluidity, liquid-gas transitions and many other systems. The properties of critical phase transtions have been discussed in detail by Stanley (1971) and Collins (1989).

The first observation of a critical phase transition was made by Andrews (1869) in CO_2. He found that for a particular pressure and temperature (p_c,T_c) there was a continuous transition from the liquid to the gaseous state. Above p_c it was not possible to distinguish the two states

and no transition could be said to occur, below p_c there was a first order transition between the two states at a temperature that varied with pressure. The critical point corresponded to the point in the (p,T) phase diagram at which the distinction between the two phases vanished.

A feature common to most phase transitions of both types is the existence of a quantity called the order parameter which is zero at temperatures above the phase transition and non-zero below it. The order parameter appears discontinuously at the transition temperature for a first order transition while it develops continuously in the case of a critical phase transition. In the case of a liquid-gas transition as in CO_2 the order parameter is the density difference between the two phases and is a scalar quantity. For critical phase transitions in magnetic systems the order parameter is the magnetization (or sublattice magnetization for antiferromagnets) and it can be a scalar or a vector of dimensionality D. The appearance of the order parameter corresponds to the breaking of a symmetry present above the transition temperature. In the rest of this section the notation and ideas used in the description of critical phase transitions in antiferromagnets will be introduced.

A crucial factor distinguishing critical phase transitions from first order transitions is that in the former case there are fluctuating regions of both phases

that exist on a microscopic scale near the critical point. These fluctuating regions have a characteristic length, ξ (the correlation length), that approaches infinity at the critical point. As a consequence of the diverging size of the fluctuating regions the response time of the system tends to infinity as the critical point is approached. This effect is known as critical slowing down.

The correlation length is not the only physical quantity that diverges at the critical point. Other quantities that become infinite include the specific heat, C_H (the subscript H denotes constant magnetic field, the relevant constraint for magnetic systems), and the isothermal susceptibility, χ_s (the subscript s denotes the sublattice susceptibility, the appropriate response function for an antiferromagnet). Since the order parameter, η (for an antiferromagnet η is the sublattice magnetization, M_s), goes to zero as the critical point is approached from below its reciprocal is also divergent at T_c (called T_N, the Néel temperature for antiferromagnets). Experimentally it is found that the diverging quantities follow a power law (Collins 1989). For example, at temperatures just above T_N the sublattice susceptibility for an antiferromagnet obeys the relation

$$\chi_s = at^{-\gamma} \qquad (1.1)$$

where a and γ are constants and t, the reduced temperature is defined by

$$t = \frac{T - T_N}{T_N} . \qquad (1.2)$$

The numerical constant γ is called a critical exponent. Critical exponents can also be defined for other diverging quantities; α for the specific heat, β for the sublattice magnetization, and υ for the correlation length, along with many others.

In general one might expect that the behaviour above and below the critical point is not the same so that below T_N equation (1.1) would become

$$\chi_s = a'(-t)^{-\gamma'} \qquad (1.3)$$

where a′ and γ' are not necessarily the same as a and γ in (1.1). While it is generally true that a $\neq$ a′, scaling theory (Kadanoff 1966) has shown that $\gamma = \gamma'$. The same is true for the other critical exponents defined above and below T_N.

Scaling theory is derived under the assumption that the functional form of the Gibbs free energy and correlation length does not depend on the length scale, L, provided L is less than the correlation length, ξ (Kadanoff 1966).

Provided that this is the case G and ξ are generalized homogeneous functions of the reduced temperature, t, and the reduced effective magnetic field,

$$h = \frac{g\mu_B H_e}{k_B T} . \tag{1.4}$$

In particular, by considering a length scale change from L to λL one obtains

$$\lambda^{d} G(t,h) = G(\lambda^{x} t, \lambda^{y} h) \tag{1.5}$$

and

$$\lambda^{1} \xi(t,h) = \xi(\lambda^{x} t, \lambda^{y} h) \tag{1.6}$$

where d is the dimensionality of the system and x and y are indices related to the critical exponents. By making use of equations (1.5), (1.6), and the results of thermodynamics various relations between the critical exponents can be derived including the equality of primed and unprimed exponents mentioned above. Relations involving only the critical exponents are termed scaling laws, for example

$$\gamma + \alpha + 2\beta = 2. \tag{1.7}$$

Relations that involve the dimensionality of the system, and hence make use of (1.5) in their derivation are called hyperscaling laws. An example is

$$\gamma + 2\beta = d\upsilon. \tag{1.8}$$

The hyperscaling relations do not apply for d > 4 (Fisher 1982). Both the scaling and hyperscaling laws are the limiting cases for inequalities that can be derived on the basis of thermodynamics alone (Griffith 1965). The Rushbrooke inequality (Rushbrooke 1963)

$$\alpha + 2\beta + \gamma \geq 2 \tag{1.9}$$

is a less restrictive version of (1.7).

Although scaling theory predicts relationships between the critical exponents it does not make any predictions as to their values. The simplest theory that does so is Ginzburg-Landau or mean-field theory in which it is assumed that the free energy, $F(T,\eta)$, can be expanded as a Taylor series in the order parameter, η, near the critical point:

$$F(T,\eta) = F_o(T) + \alpha_2(T)\eta^2 + \alpha_4(T)\eta^4 + \ldots \tag{1.10}$$

There are no odd power terms in the expansion because the energy doesn't depend on the sign of η. The condition for equilibrium is that $F(T,\eta)$ have a minimum and by applying this and making use of the fact that $\eta = 0$ above T_c and $\eta \neq 0$ below T_c it can be shown that

$$\alpha_2(T) = (T-T_c)\alpha_o \tag{1.11}$$

where α_o is a constant. Below T_c there are minima in $F(T,\eta)$ at

$$\eta = \pm \left[\frac{\alpha_o (T_c - T)}{2\alpha_4(T)}\right]^{1/2} \tag{1.12}$$

so that, neglecting the temperature dependence of $\alpha_4(T)$, the critical exponent $\beta = 1/2$. By making use of (1.10) and (1.11) other thermodynamic quantities can be calculated from the free energy and the values for the corresponding critical exponents can be derived. Ginzburg-Landau theory predicts $\gamma = 1$, $\alpha = 0$, and $\upsilon = 1/2$.

The critical exponents predicted by Ginzburg-Landau theory only satisfy the hyperscaling relation (1.8) for $d = 4$. It turns out that Ginzburg-Landau theory is only valid for $d \geq 4$ or for infinitely long range interactions (as is the case for ferroelectrics and type I superconductors due to the long ranged nature of the Coulomb interaction). This failure of the theory for most physical circumstances is not too surprising since the Taylor series expansion has been done about a point where the free energy is non-analytic and hence the expansion itself is not valid. Physically this corresponds to neglecting the fluctuations in the critical region.

The renormalization group (Wilson and Kogut 1974) method takes a similar approach to scaling theory but extends it by determining the scaling properties of a microscopic Hamiltonian. This is done under the assumption that the change in length scale affects the parameters of the Hamiltonian but not its functional form. If after n length scale transformations the length scale is $\ell^n L$ and the Hamiltonian is $\mathcal{H}_n$, a subsequent change in scale will yield a length scale $\ell^{n+1}L$ and a Hamiltonian $\mathcal{H}_{n+1}$. The change in the Hamiltonian is a transformation of the form

$$\tau(\mathcal{H}_n) = \mathcal{H}_{n+1}. \tag{1.13}$$

The correlation length of the system, ξ, is infinite at the critical point so that Hamiltonian is unchanged by a change in length scale. The critical point therefore corresponds to a fixed point of the transformation τ that has the property

$$\tau(\mathcal{H}^*) = \mathcal{H}^* \tag{1.14}$$

where $\mathcal{H}^*$ denotes the fixed point. By examining the behaviour of the Hamiltonian under the transformation τ in the vicinity of the fixed point the critical exponents of the system can be evaluated. Although renormalization group analysis can yield quite accurate preditions of the critical

exponents and critical temperature, in practice it is often quite difficult to carry out and other theoretical methods such as high temperature series expansions (Stanley 1971) and Monte Carlo simulations (Binder and Heerman 1988) are used to study critical behaviour.

One important feature of the renormalization group transformation is that with succesive iterations some of the variables in the Hamiltonian tend towards zero. Those that do are termed irrelevant variables while those that do not are relevant variables. The fact that some variables of a system may be irrelevant gives some insight into the physical origins of the universality hypothesis (Kadanoff 1971) which was actually formulated before the developement of the renormalization group. The universality hypothesis as originally formulated, states that the critical behaviour of a system depends only on three properties:

1. The dimensionality of the system, d.
2. The dimensionality of the order parameter, D.
3. Whether the forces are of long or short range. (ie. whether or not Ginzburg-Landau theory applies)

All critical phase transitions therefore should fall into universality classes according the above criteria. The exact details of the microscopic Hamiltonian beyond the above criteria are not important, they constitute irrelevant

variables. In order to include the dynamical critical behaviour it is neccesary to add a fourth criteria (Halperin et al 1972, 1974):

4. The conservation laws of the system. (e.g., whether or not the order parameter commutes with the Hamiltonian and is therefore conserved)

The universality hypothesis is of great significance because of the powerful generalizations it makes possible. Theoretical or experimental results obtained on one system can be applied to others that may be quite different in many details provided they belong to the same universality class.

1.3 Model Magnetic Systems

Since all systems that fall in the same universality class have the same critical exponents it makes sense to study the simplest possible case and generalize the results to the other members of the same class. The simplest cases are magnetic Hamiltonians of the form (Collins 1989):

$$\mathcal{H} = - \sum_{n} {\sum_{i}}' J_i \, \mathbf{S}_n \cdot \mathbf{S}_{n+i} \qquad (1.15)$$

where $\mathbf{S}_n$ is the spin at site n. J_i is the interaction coupling the spin at n with the one at n+i. The prime on the summation over the interactions is primed to indicate

that it is resticted to counting each bond once. If the spins, S_n, are three dimensional vectors then (1.15) is called the Heisenberg model. For two dimensional spins (1.15) is called the XY model while for one dimensional spins it is called the Ising model.

Model magnetic systems are physical realizations of the simple magnetic Hamiltonians often dealt with theoretically. The spins, S_n, correspond to the magnetic moments that come from unpaired electron spins and orbital angular momentum of valence electrons of ions in solids. The interactions, J_i, are the coupling between these moments. These can arise from the long range, dipolar, interaction. This is usually weak compared to exchange interaction, which is due to the overlap of the orbitals of neighbouring atoms and the Pauli exclusion principle. If the exchange interaction is mediated by additional ions then it is referred to as a superexchange interaction. Exchange and superexchange interactions are short ranged, often restricted to nearest neighbours. In metals spin-spin interactions can also be mediated by the conduction electrons, this is known as the RKKY interaction.

In real systems there can also be additional terms in the Hamiltonian such as external magnetic fields or anisotropies that favour the alignment of the spins along a particular axis or plane. These can occur as a result of the dipolar interaction (which favours spins aligned

perpendicular to the line connecting them) or the effect of the crystalline electric field on the orbital angular momentum. If such an anisotropy is present, then there will be a crossover from a regime at high temperatures where the spins are three dimensional vectors to one at lower temperatures where the spins are two or one dimensional vectors depending on whether the anisotropy is uniaxial or planar.

It is the interaction between the spins that is responsible for the transition to long range magnetic order. If J is positive then it favours parallel or ferromagnetic alignment of the spins it couples. If J is negative then it favours antiparallel or antiferromagnetic alignment of the spins it couples. If we now restict the discussion to the simple case of nearest neighbour interactions on a two dimensional square lattice, then the type of ordered structures that occur are shown in Figure 1.1.A for $J > 0$ and 1.1.B for $J < 0$. The direction of the spins with respect to the lattice is arbitrary and it is this rotational symmetry that is broken by the phase transition when one direction is selected.

It is easy to see that for all lattices in all dimensions the ferromagnetic structure with all spins parallel will satisfy nearest neighbour interactions with $J > 0$. For antiferromagnetic interactions ($J < 0$) it is not always possible to find a magnetic structure in which all

A J > 0 B J < 0

Figure_1.1: Magnetic structure for nearest neighbour interactions on a square lattice. In case A (J > 0) there is ferromagnetic ordering and in case B (J < 0) there is antiferromagnetic ordering.

nearest neighbour spins are antiparallel. Consider the case of a triangular lattice in two dimensions illustrated in Figure 1.2. Two spins are aligned antiparallel, it is not possible to orient the spin on the third site so that it is simultaneously antiparallel to both the others. This effect is known as lattice frustration because there are bonds for which the interaction energy is not minimized; the

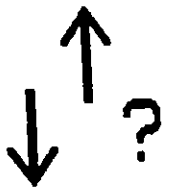

Figure_1.2: If two spins on a triangular lattice with antiferromagnetic interactions are aligned antiparallel it is not possible to orient the spin on the third site such that both bonds to the other spins are satisfied.

interactions are "frustrated". Lattice frustration occurs in any system with antiferromagnetic nearest neighbour interactions on a lattice where there are nearest neighbours of a site that are nearest neighbours of each other. Frustration can also occur in systems where there are longer ranged interactions that favour a different structure than the nearest neighbour ones or in systems where there are random interactions. Frustrated magnetic systems exhibit a rich variety of behaviour such as spin glass transitions and complicated non-collinear magnetic structures for less frustrated cases. For the triangular lattice considered above, a non-collinear magnetic structure will result if the spins are continuous (ie. $D \geq 2$). In the ground state the spins make 120° angles with one another so that, while no bond is entirely satisfied none is completely frustrated. There are two degenerate configurations that differ in the sense of the rotation of the spins moving around the triangle or the chirality as shown in Figure 1.3. This chiral degeneracy is in addition to the degeneracy

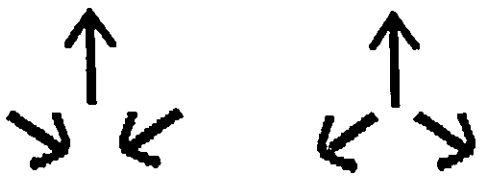

Figure 1.3: The two degenerate configurations of the 120° structure for the triangular antiferromagnet.

associated with global rotation of the spins with respect to the lattice mentioned previously for the square lattice.

The presence of this additional degeneracy gives rise to associated fluctuations that may disrupt the long range order. These fluctuations take the form of Ising-like domain walls between regions of differing chirality. The long range order can also be disrupted by spin waves as in unfrustrated systems. Because it is the fluctuations in a system that govern its critical properties it has been suggested (Kawamura 1988a) that triangular antiferromagnets should belong to universality classes distinct from the conventional ones. The new universality classes would be defined by the symmetry of the order parameter, not just by its dimensionality. Using this criteria the XY triangular antiferromagnet would belong to the $Z_2 \times S_1$ universality class where the Z_2 denotes the Ising-like chiral degeneracy the S_1 denotes the XY degeneracy. Similarly the Heisenberg triangular antiferromagnet would belong to the SO(3) universality class rather than the S_2 universality class of the unfrustrated case.

Because the triangular antiferromagnets belong to new universality classes, they should have their own characteristic critical exponents. Monte Carlo simulations (Kawamura 1989) and renormalization group analysis (Kawamura 1988b) have been used to study the critical behaviour of the XY triangular antiferromagnet and the results along with the

predictions for the standard XY model (S_1) (Baker et al 1978), are summarized in Table I. The predicted exponents for the $Z_2 \times S_1$ universality class differ significantly from those of the XY model, particularly the value for α which is close to zero for the XY model but has the very large positive value of 0.4 for the $Z_2 \times S_1$ case.

Exponent	$Z_2 \times S_1$	S_1
γ	1.1 ± 0.1	1.316 ± 0.009
υ	0.53 ± 0.03	0.669 ± 0.007
β	0.25 ± 0.02	0.345 ± 0.011
α	0.40 ± 0.04	-0.01

Table I: Critical exponents γ, υ, β, and α for the $Z_2 \times S_1$ universality class (Kawamura 1989) and the standard XY model (S_1) (Baker et al 1978)

Similar exponents are predicted for the SO(3) universality class (Kawamura 1988a) and these are shown along with the predictions for the Heisenberg model (S_2) (Collins 1989) and the measured exponents for VCl_2 (Kadowaki et al 1987), a Heisenberg triangular antiferromagnet, in Table II. The values obtained in the neutron scattering measurements of Kadowaki et al (1987) are in good agreement with the predictions for the SO(3) universality class and substantially different from those expected for the standard Heisenberg model that applies to the nonfrustrated case.

Exponent	SO (3)	S_2	VCl_2
γ	1.1 ± 0.1	1.388 ± 0.003	1.05 ± 0.03
υ	0.55 ± 0.03	0.707 ± 0.003	0.62 ± 0.05
β	0.28 ± 0.02	0.367 ± 0.005	0.20 ± 0.02

Table II: Critical exponents γ, υ, and β for the SO(3) universality class (Kawamura 1988a), the standard Heisenberg model (S_2) (Collins 1989) and the experimental values for the Heisenberg triangular antiferromagnet VCl_2 (Kadowaki et al 1987).

The predicted set of critical exponents for both frustrated cases are not the same as those for any system that can be described by the standard universality hypothesis as described earlier in this chapter.

1.4 Structural and Magnetic Properties of $CsMnBr_3$

$CsMnBr_3$ is an insulating compound with a hexagonal crystal structure belonging to the space group $P6_3/mmc$. At room temperature a = 7.61 Å and c = 6.52 Å (Goodyear and Kennedy, 1974). The crystal structure of is shown in Figure 1.4. The Mn^{+2} ions in $CsMnBr_3$ form a simple hexagonal lattice with a Mn-Mn separation of 3.26 Å along the c axis and 7.61 Å in the ab plane. As is evident from Figure 1.4 the superexchange path for the Mn ions along c is shorter and less complicated than within the ab plane. Consequently the antiferromagnetic interaction between the spin $\frac{5}{2}$ Mn^{+2} moments is 460 times stronger along c than in the ab plane

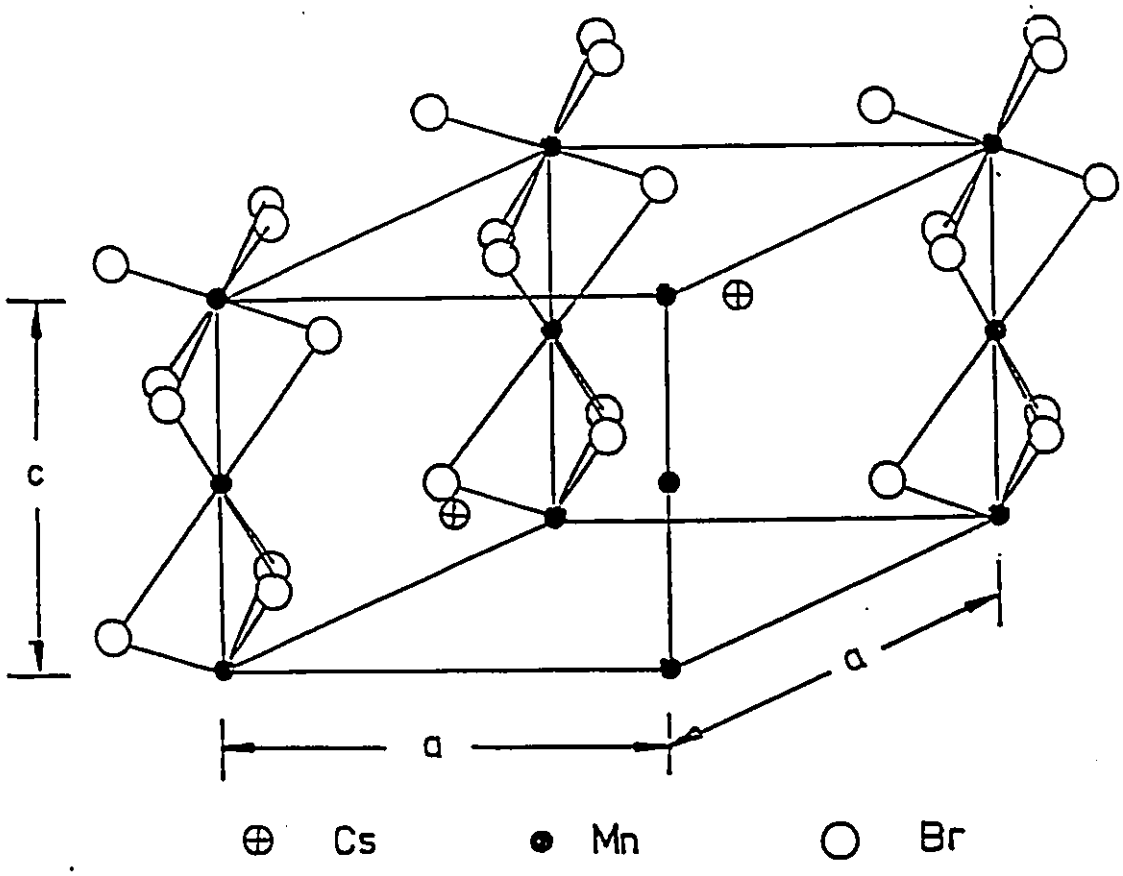

Figure 1.4: Crystal structure of $CsMnBr_3$ (from Gaulin 1986)

(Gaulin et al 1987). This results in quasi-one-dimensional behaviour above about 15 K (Gaulin and Collins 1984, Gaulin 1986, Fitzgerald et al 1982). The spins are restricted to the ab plane below about 20 K by an anisotropy that is primarily dipolar in origin.

$CsMnBr_3$ undergoes a critical phase transition to long range three dimensional order at 8.3 K (Eibshutz et al 1973). The magnetic structure of the ordered state is the 120° structure described above with the spins in the ab plane. The maximum ordered moment has been determined experimentally to be $(3.0 \pm 0.3)\mu_B$ (Eibshutz et al 1973), reduced from the $5\mu_B$ expected for spin $\frac{5}{2}$ by quantum fluctuations in the frustrated state. The magnetic Hamiltonian for $CsMnBr_3$ has been determined from inelastic neutron scattering measurements of spin waves in the ordered state (Gaulin et al 1987, Falk et al 1987) to be :

$$\mathcal{H} = -2J_c \sum_{i>j} \mathbf{S}_i \cdot \mathbf{S}_j - 2J_{ab} \sum_{i>j} \mathbf{S}_i \cdot \mathbf{S}_j + D \sum_i (S_i^z)^2 \qquad (1.16)$$

where the interaction between nearest neighbour spins along the c axis, J_c, is -0.88 ± 0.01 meV; the interaction between nearest neighbour spins in the ab plane, J_{ab}, is -0.0018 ± 0.0001 meV and the planar anisotropy, D, is 0.013 ± 0.001 meV.

Because the magnetic ions in $CsMnBr_3$ form a simple

hexagonal lattice and the spins are restricted to two dimensions the critical phase transition at 8.3 K is expected to belong to the $Z_2 \times S_1$ universality class. Since this compound is an insulator with only nearest neighbour interactions, its Hamiltonian is relatively simple making it a good candidate for investigations to determine the effects of the additional chiral degeneracy on the critical properties.

CHAPTER 2

NEUTRON SCATTERING

2.1 Magnetic Neutron Scattering Formalism

In order to study the microscopic behaviour of magnetic materials, a probe that is well matched to the system under study, in terms of wavelength and energy, is desirable. The neutron, available as a product of the nuclear chain reaction in a reactor, has these properties. The spectrum of thermal neutrons around the core of a reactor has a Maxwellian distribution characteristic of the temperature of the moderator. This is typically around 300 K, corresponding to an energy, $k_B T_m$ = 6.2 THz = 25.9 meV (1 THz = 4.136 meV). The wavelength of the neutron in Ångstroms is related to its energy in THz by:

$$\lambda = \sqrt{\frac{19.78}{E}} \qquad (2.1)$$

so the wavelength for a 6.2 THz neutron is 1.79 Å. The wavelength and energy of a thermal neutron is therefore comparable to the interatomic spacings and excitation energies found in solids.

Neutrons interact with solids through the short

ranged strong force that couples the neutron and the nuclei of the material under study. In magnetic materials the long range dipolar interaction couples the magnetic moments in the solid to that of the neutron. This interaction is weaker than the nuclear interaction but because of its longer range, the mean free path for both types of events is comparable, about 1 cm. The neutron scattering formalism is covered in great detail in books devoted to that topic (Squires 1978, Lovesey 1984). This chapter will summarize the results relevant to the present work.

In a neutron scattering experiment the quantity measured is the partial differential cross section; the probability of scattering into a solid angle $d\Omega$ in a scattered energy range dE'. For a system of N identical nuclei with a scattering length b, the partial differential cross section for coherent scattering is

$$\frac{d^2\sigma}{d\Omega dE'} = \frac{k'}{k} Nb^2 S(Q,\omega) \qquad (2.2)$$

where $\hbar\mathbf{k}$ and $\hbar\mathbf{k}'$ are the initial and final neutron momenta, $\mathbf{Q}$ is the scattering vector ($\mathbf{Q} = \mathbf{k} - \mathbf{k}'$), and ω is the energy transfer ($\hbar\omega = E - E'$). $S(Q,\omega)$ is the scattering function, the space and time Fourier transform of the nuclear correlation function

$$S(\mathbf{Q},\omega) = \frac{1}{hN} \sum_{j1} \int_{-\infty}^{\infty} \exp(i\omega\tau)\, d\tau$$
$$\times \langle \exp(-i\mathbf{Q}\cdot\mathbf{R}_1(0)) \exp(i\mathbf{Q}\cdot\mathbf{R}_j(\tau)) \rangle \qquad (2.3)$$

where $\mathbf{R}_j(\tau)$ is the position vector of the j^{th} atom at time τ.

The magnetic partial differential cross section for scattering from N identical magnetic atoms has a similar form to (2.2)

$$\frac{d^2\sigma}{d\Omega dE'} = \frac{k'}{k}\frac{N}{h} (\gamma r_o)^2 \, |F(\mathbf{Q})|^2 \sum_{\alpha\beta} (\delta_{\alpha\beta} - \hat{Q}_\alpha \hat{Q}_\beta) \, S^{\alpha\beta}(\mathbf{Q},\omega) \qquad (2.4)$$

where the length $\gamma r_o = 5.391$ fm is analogous to the nuclear scattering length, b. $F(\mathbf{Q})$ is the magnetic form factor. It arises due to the finite spatial extent of the magnetic moment distribution and is a characteristic of the magnetic ion that scatters the neutron. The polarization factor, $(\delta_{\alpha\beta} - \hat{Q}_\alpha \hat{Q}_\beta)$, reflects the fact that the scattering is from the components of the moment perpendicular to the scattering vector. The scattering function is a second rank tensor. If the atomic positions are fixed then $S^{\alpha\beta}(\mathbf{Q},\omega)$ is the space and time Fourier transform of the spin-spin correlation function (between α and β components)

$$S^{\alpha\beta}(\mathbf{Q},\omega) = \frac{1}{2\pi} \sum_{\mathbf{R}} \exp(i\mathbf{Q}\cdot\mathbf{R})$$
$$\times \int_{-\infty}^{\infty} \exp(i\omega\tau) \; \langle S_{0\alpha}(0) \; S_{\mathbf{R}\beta}(\tau) \rangle \, d\tau \qquad (2.5)$$

where $S_{\mathbf{R}\beta}(\tau)$ is the β component of the spin at $\mathbf{R}$ at time τ. Generally the symmetry of most materials ensures that only the diagonal elements, $S^{\alpha\alpha}(\mathbf{Q},\omega)$, contribute.

2.2 Magnetic Critical Scattering

Equations (2.4) and (2.5) above are quite general. The usefulness of magnetic neutron scattering for the study of magnetic phase transitions arises from two special cases for the cross section (Cowley 1987, Collins 1989). If the magnetic scattering function is integrated over energy one obtains:

$$\int_{-\infty}^{\infty} S^{\alpha\beta}(\mathbf{Q},\omega) \; d\omega = \sum_{\mathbf{R}} \exp(i\mathbf{Q}\cdot\mathbf{R}) \; \langle S_{0\alpha} S_{\mathbf{R}\beta} \rangle = C^{\alpha\beta}(\mathbf{Q}) \qquad (2.6)$$

where $C^{\alpha\beta}(\mathbf{Q})$ is the static correlation function. Near a critical phase transition it depends on the reduced temperature, t, and the reduced magnetic field, h (ie. $C^{\alpha\beta}(\mathbf{Q}) = C^{\alpha\beta}(\mathbf{Q},t,h)$). If all the weight of the scattering function is at low frequencies ($\hbar\omega << E$) then the static correlation function can be obatined by measuring the differential cross section (Collins 1989). The probability

of scattering into a solid angle $d\Omega$ independent of final energy E' in this case is

$$\frac{d\sigma}{d\Omega} = \frac{N}{h} (\gamma r_o)^2 \, |F(Q)|^2 \sum_{\alpha\beta} (\delta_{\alpha\beta} - \hat{Q}_\alpha \hat{Q}_\beta) \, C^{\alpha\beta}(Q,t,h). \qquad (2.7)$$

The approximation $\hbar\omega << E$ necessary to obtain this result is called the static approximation. The real space static correlation function, $C^{\alpha\beta}(R,t,0)$, for $T > T_c$ is well approximated by (Ornstein and Zernike 1914, Fisher 1964, Fisher and Burford 1967)

$$C(R,t,0) \; \alpha \; |R|^{(1-d)/2} \, \xi^{(3-d)/2-\eta} \exp(|R|/\xi). \qquad (2.8)$$

For three dimensional systems η is close to zero (eg. η = 0.03 for the three dimensional XY model) and the Fourier transform of (2.8) becomes a Lorentzian (Ornstein and Zernike 1914)

$$C(Q,t,0) \; \alpha \; \frac{1}{q^2 + \kappa_1^2} \qquad (2.9)$$

where κ_1 is the inverse correlation length, ξ^{-1}, and q is the displacement from the ordering wavevector, $q = Q - Q_o$. An approximateform that includes η and has the correct form at the critical temperature is (Fisher and Burford 1967)

$$C(Q,t,0) \propto \frac{1}{(\psi q^2 + \kappa_1^2)^{1-\eta/2}} \qquad (2.10)$$

where $\psi = (1-\eta/2)^{-1}$. This is a broad peak that appears in the neutron cross-section near the critical temperature. It is called critical scattering. By determining the temperature dependence of its width one can obtain ξ and hence υ. The peak intensity can be used to determine γ since

$$C(Q_o,t,0) \propto \chi(Q_o) \ . \qquad (2.11)$$

The second special case of interest in the study of critical phenomena is the spin correlation function for infinite time, $<S_{0\alpha}(0)S_{R\beta}(\infty)>$. In the paramagnetic state this will be zero but below the critical temperature there is order for all time so it will be non zero. This gives rise to an elastic ($\omega = 0$) part of the cross section

$$S^{\alpha\beta}_{el}(Q,\omega) = \delta(\omega) \sum_R \exp(iQ\cdot R) \ <S_{0\alpha}(0)S_{R\beta}(\infty)> \qquad (2.12)$$

which is proportional to the square of the order parameter. The temperature dependence of the elastic (Bragg peak) intensity can therefore be used to obtain the critical exponent β.

2.3 Triple-Axis Neutron Spectrometry

In order to measure the scattering function, $S(\mathbf{Q},\omega)$, one needs an instrument capable of measuring the scattered neutron intensity systematically in the four dimensional space spanned by $\mathbf{Q}$ and ω. The triple-axis spectrometer, first developed by Brockhouse (1961), has this capability. Nuclear Bragg scattering (analogous to the magnetic Bragg scattering of equation (2.12)) is used to select the incident neutron energy and determine the scattered neutron energy. This means there are actually three scattering events; one to produce a monochromatic beam, one at the sample, and one to analyze the scattered neutron energy; hence the name triple-axis.

Nuclear Bragg scattering is an elastic scattering process that occurs when the momentum transfer, $\mathbf{Q}$, is equal to a reciprocal lattice vector $\mathbf{G}$. This means that the scattering function contains terms

$$\delta(\omega) \sum_{\mathbf{G}} \delta(\mathbf{Q}-\mathbf{G}) \tag{2.13}$$

This condition will be satisfied if

$$G = 2k \sin(\tfrac{\phi}{2}) \tag{2.14}$$

which is Bragg's law, where ϕ is the angle between $\mathbf{k}$ and $\mathbf{k}'$. A more familiar form is

$$\lambda = 2d \sin\theta \qquad (2.15)$$

where $\theta = \phi/2$, λ is the wavelength of the neutrons, $\lambda = 2\pi/k$, and d is the spacing between the planes in the crystal, $d = 2\pi/G$. Equation (2.15) can be used to determine the scattering angle necessary to extract a beam of a given wavelength (and hence energy) from the Maxwellian spectrum emanating from the core of a reactor. The d spacing is determined by the crystal used and the particular reflection selected. The (111) reflection from Si and the (002) reflection from pyrolytic graphite (PG) are often chosen to produce a monochromatic beam. The same process is used to analyze the final energy of the scattered beam.

The layout of a triple-axis spectrometer is shown schematically in Figure 2.1. The scattering angles at the monchromator and the analyzer are denoted $2\theta_M$ and $2\theta_A$ respectively. The scattering angle at the sample is called ϕ while the orientation of the sample with respect to the incident beam is called ψ. The divergence of the beam along its flight path is controlled by Soller slit collimators which use vertical slits coated with a neutron absorbing material such as Cd to control the angular divergence in front of a particular element of the spectrometer. The detector counts the pulses produced in a ^4He-^3He mixture from the capture of a neutron by a ^3He nucleus.

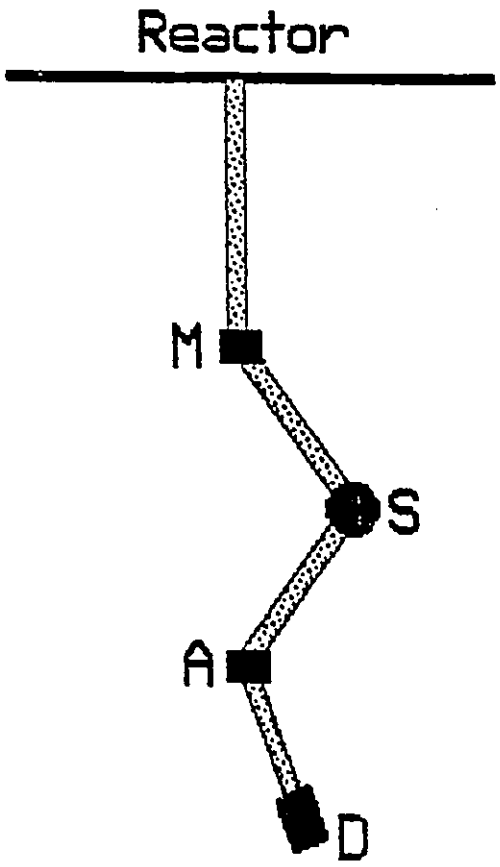

Figure 2.1: Schematic diagram of a triple-axis spectrometer indicating the monochromator (M), sample (S), analyzer (A), and detector (D).

The static correlation function can be measured in the static approximation (equation (2.7)) by removing the analyzer crystal and positioning the detector directly in the beam scattered from the sample. In this way all the neutrons scattered in a given direction will be detected. By setting the analyzer for the same energy as the incident beam one measures the elastic scattering cross section (equation (2.12)). Generally the sample is oriented with a high symmetry axis perpendicular to the horizontal scattering plane. By rotating the sample about this axis, momentum transfers within the plane defined by the vertical axis can be selected.

Bragg's law (equation (2.15)) can be satisfied at a given scattering angle by more than one wavelength of neutrons. If ϕ is set so that neutrons of wavelength λ will scatter from planes spaced by d, then neutrons of wavelength λ/n (and energy n^2E) will be scattered by planes spaced by d/n (ie. the scattering angle for the (002) reflection of PG for λ is the same as the scattering angle for the (004) reflection for $\lambda/2$)). In order to remove this higher order contamination one can select monochromator or analyzer crystals for which the higher index reflection is absent due to the symmetry. For example the (111) reflection of Si is a strong Bragg peak while the (222) reflection is absent so there will be no $\lambda/2$ contamination from Si (111). Alternatively, a filter that passes the neutrons of

wavelength λ but attenuates those with shorter wavelengths, may be placed in the beam. PG oriented with the c axis along the beam direction transmits neutrons with $\lambda = 2.37$ Å while strongly attenuating neutrons with wavelengths $\lambda/2$ and $\lambda/3$ (Loopstra 1966, Shirane and Minkiewicz 1970).

Real crystals are not perfect, but consist of small crystallites slightly misoriented with respect to one another. This mosaic spread, typically a few tenths of a degree, means that the Bragg condition can be satisfied over a range of angles. The mosaic spread of the monochromator and analyzer (and also the sample if a single crystal is being studied) together with the finite angular divergence of the beam as defined by the collimators, determine the resolution of the spectrometer (Cooper and Nathans 1967, Nielsen and Möller 1969). The resolution function for a triple-axis spectrometer is an ellipsoid of constant intensity contours in the four dimensional $(\mathbf{Q},\omega)$ space with a profile that is approximately Gaussian. Because vertical slits are used to collimate the beam the resolution perpendicular to the scattering plane is much coarser than it is in the plane. This is done deliberately to increase the intensity without unduly sacrificing resolution in the scattering plane.

Because of the finite resolution of the spectrometer what one actually measures in an experiment is the convolution of the scattering function with the resolution

function

$$I(Q,\omega) \propto \int S(Q-Q',\omega-\omega')\, R(Q',\omega')\, d\omega'\, d^3Q' \qquad (2.16)$$

In cases where one is interested in the detailed lineshape of $S(Q,\omega)$, such as measurements of C(Q,t,h), it is necessary to include the effects of the resolution. One can determine the resolution experimentally by looking at a Bragg peak for which

$$S(Q,\omega) \propto \delta(\omega)\, \delta(Q-Q_o) \qquad (2.17)$$

Substituting (2.17) into (2.16) one sees that the measured intensity is just the resolution

$$I(Q,\omega) \propto R(Q-Q_o,\omega) \qquad (2.18)$$

in the vicinity of the Bragg peak.

CHAPTER 3

CRITICAL EXPONENTS OF $CsMnBr_3$

3.1 Introduction

This chapter describes measurements of the static critical exponents; γ, υ, and β in $CsMnBr_3$ carried out using the neutron scattering techniques described in Chapter 2. The measurements were done using the L3 triple axis spectrometer of the NRU reactor at Chalk River Nuclear Laboratories.

The (111) reflection from silicon was used to monochromate the beam and the (002) reflection from pyrolytic graphite was used to analyze the scattered beam for the elastic and inelastic measurements. The critical scattering above T_N was measured in double axis mode so as to integrate over the energy transfer. The mosaic spreads of the monochromator and the analyzer were 0.2° and 0.4° respectively. The collimation was 1.1° from the source to the monochromator, 0.3° from the monochromator to the sample and the sample to the analyzer, and 2.6° from the analyzer to the detector. The vertical collimation was 1.3°. For the critical scattering and the elastic scattering a neutron energy of 3.3 THz was used so that a pyrolytic graphite filter could be placed in the scattered beam to remove

higher order contamination.

The inelastic scans were done with the final energy (E′) fixed. In this mode the measured intensity is proportional to $S(Q,\omega)$ since the efficiency of the incident beam monitor used to normalize the incident neutron flux varies as k^{-1} (therefore the factor of k'/k in equation (2.4) drops out). The value of E′ used was determined by the energy resolution required.

The crystal of $CsMnBr_3$ was grown at Oak Ridge National Laboratory by Dr. B.D. Gaulin from stoichiometric amounts of CsBr and $MnBr_2$ by standard Bridgeman techniques. Great care was taken to eliminate impurities so as to avoid any effect on the critical properties. The crystal was irregular in shape with approximate dimensions $2 \times 1 \times 0.6$ cm^3. Figure 3.1 is a rocking curve for the (002) nuclear Bragg reflection. If the sample was a perfect crystal the profile would be approximately Gaussian with a full width at half maximum (FWHM) that depends primarily on the collimation between the monochromator and the sample and the monochromator mosaic spread. Figure 3.1 shows that the sample actually consists of two main crystallites separated by about 0.95°. Each of the peaks has a FWHM of 0.5°, larger than the expected width, 0.3°, indicating mosaic spread within the crystallites.

The sample was mounted in a helium cryostat with (ξ,ξ,ζ) in the scattering plane. The temperature was

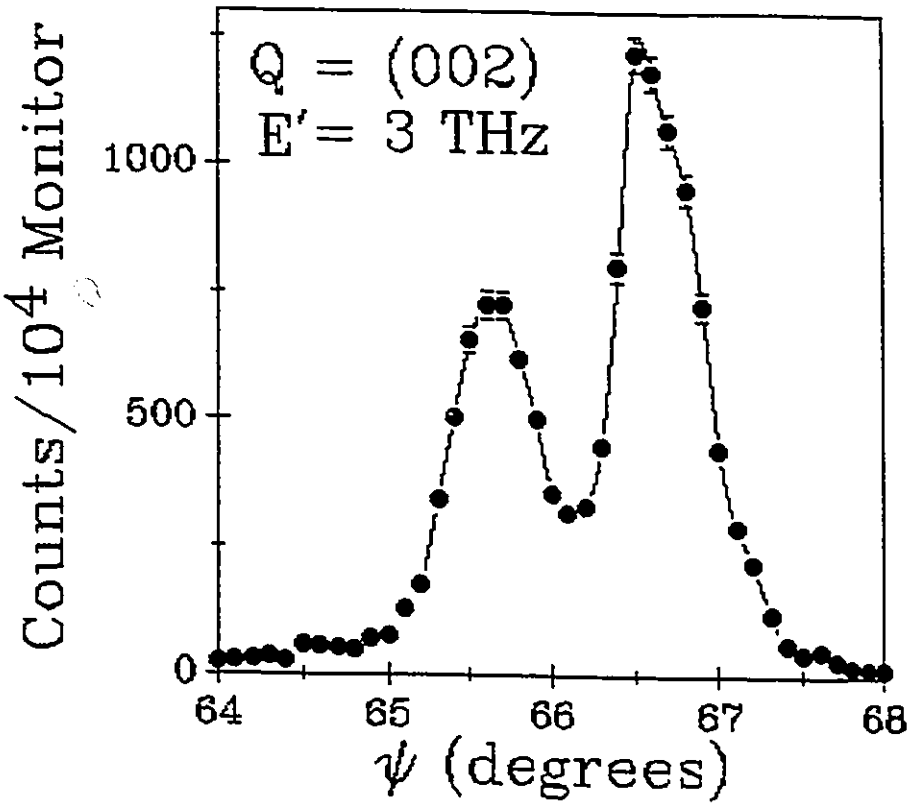

Figure_3.1: Rocking curve (ψ is the sample angle) about the (002) reflection of $CsMnBr_3$.

monitored using a germanium sensor mounted on the heater block. The sample was in an aluminum can filled with helium gas to ensure good thermal contact. The temperature was computer controlled and stable to ± 0.02 K.

The measurements described in this chapter have been reported in the scientific literature (Mason et al 1987, Gaulin et al 1989a, and Mason et al 1989).

3.2 Paramagnetic Critical Scattering

Near the critical temperature the correlated regions of spins give rise to critical scattering with the Lorentzian lineshape of equation (2.9). In order to measure the energy-integrated intensity in double-axis mode it was necessary to check the validity of the static approximation for the incident neutron energy used (3.3 THz). Because changes in the length of the scattered neutron wavevector, k', (and hence energy) involve changes in the momentum transfer, Q, the static approximation will break down if the characteristic energy of the critical scattering is large compared to the incident neutron energy.

Figure 3.2 shows two triple-axis constant-Q scans near the ordering wavevector $(\frac{1}{3},\frac{1}{3},1)$ close to T_N. The top panel at (.38,.38,1) for T = 9 K, shows a relatively sharp peak centred on frequency, $\upsilon = 0$, due to the incoherent elastic scattering and a broad shoulder of critical scattering that falls off below about $\upsilon = .35$ THz. The

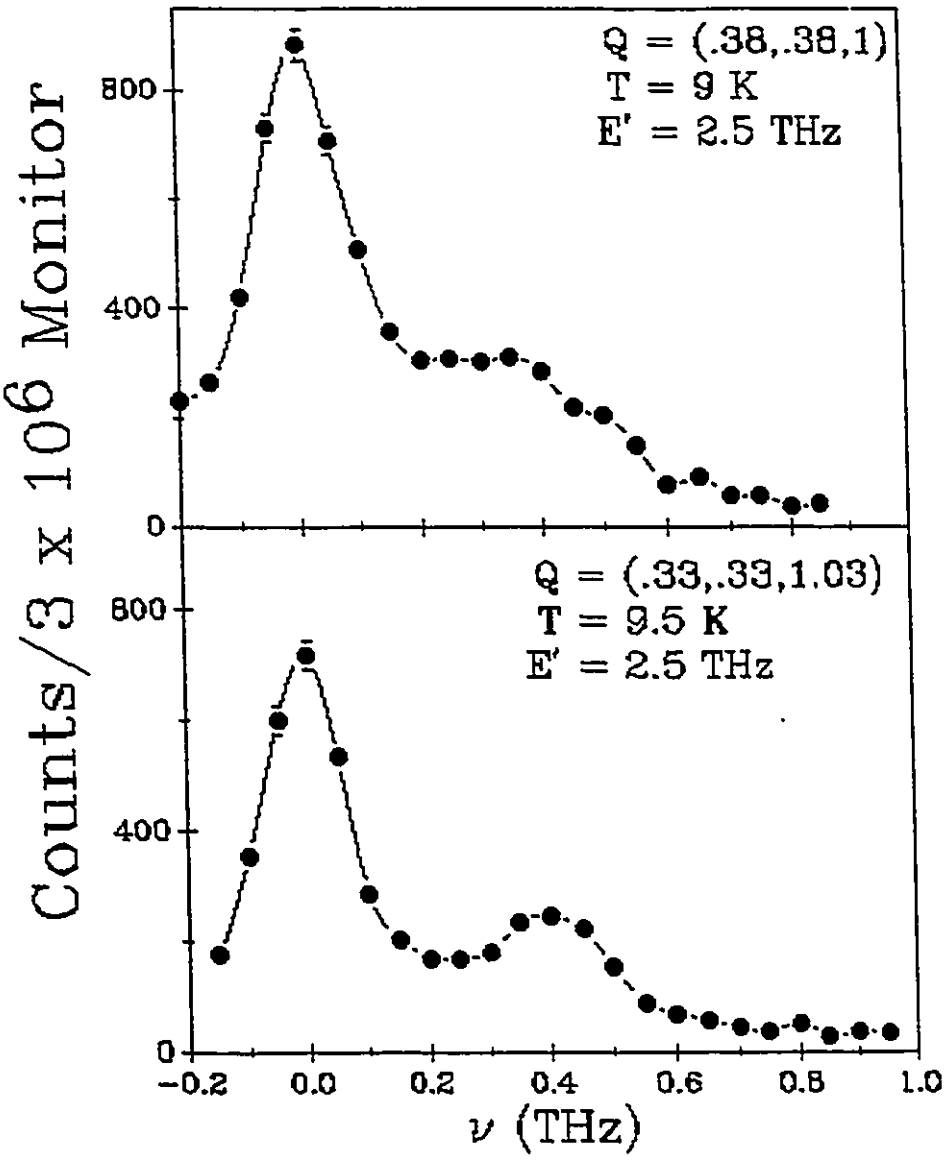

Figure 3.2: Constant-Q scans at (.38,.38,1) and (.33,.33,1.03).

bottom panel shows a similar scan at (.33,.33,1.03) for T = 9.5 K.

A detailed analysis by Tucciarone et al (1971) has shown that the static approximation will be valid for a given scan provided the quantity

$$\alpha = \frac{m}{8\hbar^2 E_1}\left[\frac{\hbar\Gamma_\kappa}{\kappa_1}\kappa\right]^2, \qquad (3.1)$$

where Γ_κ is the characteristic energy at a distance κ_1 from the antiferromagnetic zone centre, is smaller than 1. For the scan in the ab-plane at T = 9.0 K the inverse correlation length is $\cong$ 0.07 Å^{-1}. Assuming the characteristic energy decreases linearly as the zone centre is approached, Γ_κ would be about 0.26 THz at 9.0 K (since the characteristic energy is 0.35 THz at (0.38,0.38,1)). Using these parameters one obtains an estimate of $\alpha \cong 0.5$ indicating the static approximation is valid for this case. For the scans along the c axis the peak centred on 0.39 THz in the bottom scan of Figure 3.2 will not be fully integrated but this is the gapped mode of the quasi-one-dimensional phase which does not correspond to the Goldstone mode. The lower frequency fluctuations that are near the central peak of the scan do go soft at the phase transition and these are correctly integrated.

Similar scans were performed at various momentum

transfers and temperatures throughout the range of the measurements described below and the static approximation was found to hold quite generally for this configuration. The critical exponents determined in this way (see below) have been confirmed by measurements using a neutron energy of 16.3 THz and different ordering wavevector $((\frac{1}{3},\frac{1}{3},3))$ (Kadowaki et al 1988) indicating that the present configuration was adequate.

The critical scattering above T_N was measured in scans along $(\xi,\xi,1)$ from $\xi = 0$ to $\xi = 1$ and along $(\frac{1}{3},\frac{1}{3},\zeta)$ from $\zeta = 0.92$ to $\zeta = 1.08$ for twelve temperature between 8.45 K and 11.90 K. Figure 3.3 shows the scans in reciprocal space. The crossed and solid circles are strong and weak nuclear Bragg peaks respectively and the open circles are the magnetic ordering wavevectors $(\frac{1}{3},\frac{1}{3},1)$ and $(\frac{2}{3},\frac{2}{3},1)$. The inset shows the relative positions of the two crystallites about $(\frac{1}{3},\frac{1}{3},1)$ as determined from a mesh of scans over the magnetic Bragg peak at 4.2 K, well below T_N. This information along with similar scans about $(\frac{2}{3},\frac{2}{3},1)$ was used to define the resolution function necessary for the analysis of section 3.4.

Figure 3.4 shows the data for three temperatures, 8.45 K, 8.83 K, and 10.90 K. The lines are the results of fits described in section 3.4. The temperature for each pair of scans was determined by averaging the temperature readings for each point over the peak in the critical

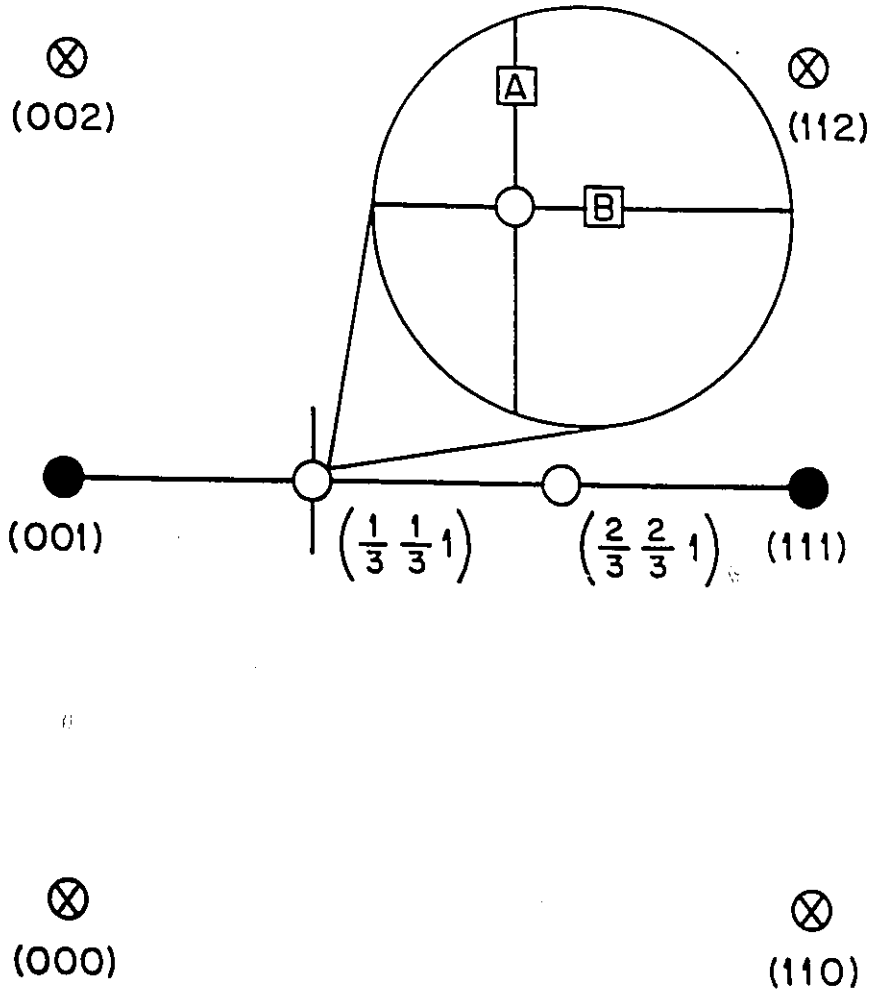

Figure 3.3: Scans in reciprocal space for critical scattering above T_N. The solid and crossed circles are nuclear Bragg reflection, the open circles are the magnetic ordering wavevectors.The inset shows the relative positions of the two crystallites (denoted A and B) relative to the scans.

scattering. The fluctuations in the temperature readings were used to estimate the uncertainty in the temperature. The uncertainty in the scattered intensity is the square root of the number of counts due to the statistical nature of the scattering process. As T_N is approached from above the critical scattering grows in intensity and decreases in width. The right and left panels of Figure 3.4, corresponding to scans in the ab-plane and along the c-axis, have quite different x axis scales reflecting the much narrower peak for the scans along c. This arises because the spins are already well correlated within the chains upon entering the three dimensional critical regime as a consequence of the much stronger interactions in that direction. The width of the peak in the c direction is about twice that of the experimental resolution at the lowest temperature (8.45 K). The width in the ab-plane is about ten times larger than the resolution for the same temperature.

3.3 Elastic Magnetic Scattering

Measurements of the magnetic Bragg peak intensity as a function of temperature have been carried out in triple axis mode with the analyzer set for elastic scattering. The peak intensities for three peaks; $\mathbf{Q} = (\frac{1}{3},\frac{1}{3},1)$, $(\frac{1}{3},\frac{1}{3},3)$, and $(\frac{4}{3},\frac{4}{3},1)$. Figure 3.5 shows the temperature dependence of the $(\frac{1}{3},\frac{1}{3},1)$ peak. The line is the result of the fit described

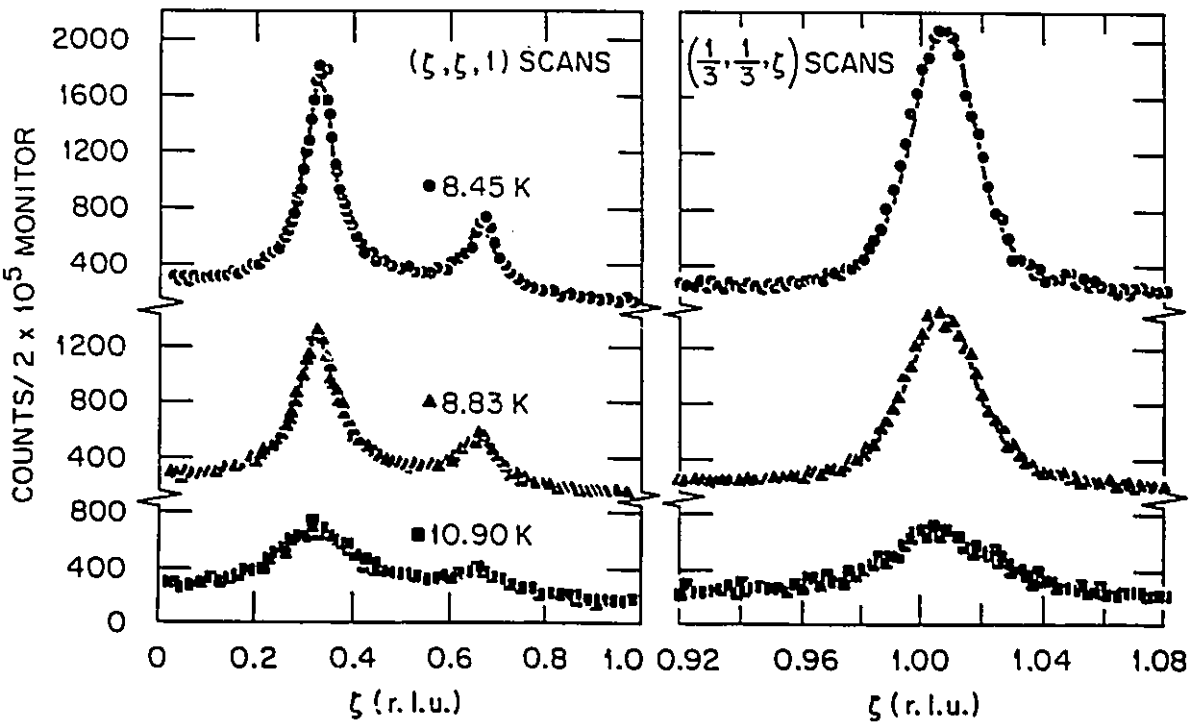

Figure 3.4: Measured critical scattering along $(\xi,\xi,1)$ and $(\frac{1}{3},\frac{1}{3},\zeta)$ (in reciprocal lattice units) for T = 8.45 K, T = 8.83 K, and T = 10.90 K. The lines are the fits to a Lorentzian convoluted with the spectrometer resolution function described in section 3.4

in section 3.4. For each temperature the peak intensity was determined by averaging at least five counting intervals after the intensity had ceased evolving with time, indicating the sample had reached equilibrium.

The phase transition is marked by a sharp onset of the Bragg peak intensity at about 8.3 K. The sharpness of the transition indicates that the sample temperature was at least as uniform as it was stable. There is also a small increase in the background above T_N due to a small contribution from critical scattering within the finite energy resolution of the spectrometer.

The three peaks measured had scattering angles of 25.0°, 70.5°, and 56.2° respectively. The ratio of the intensities was 11:2.5:1. The effects of extinction on the peak intensities would be quite different due to the wide range of scattering geometries and intensities. The fact that the ratio of the intensities remained constant, within experimental uncertainty, over the whole range of temperatures measured (from 4.2 K to T_N) indicates that extinction effects were not significant for this crystal. This is a consequence of the rather poor mosaic of the sample.

3.4 Data Analysis

In order to extract the values for the sublattice susceptibility, χ, and the inverse correlation length, κ_1,

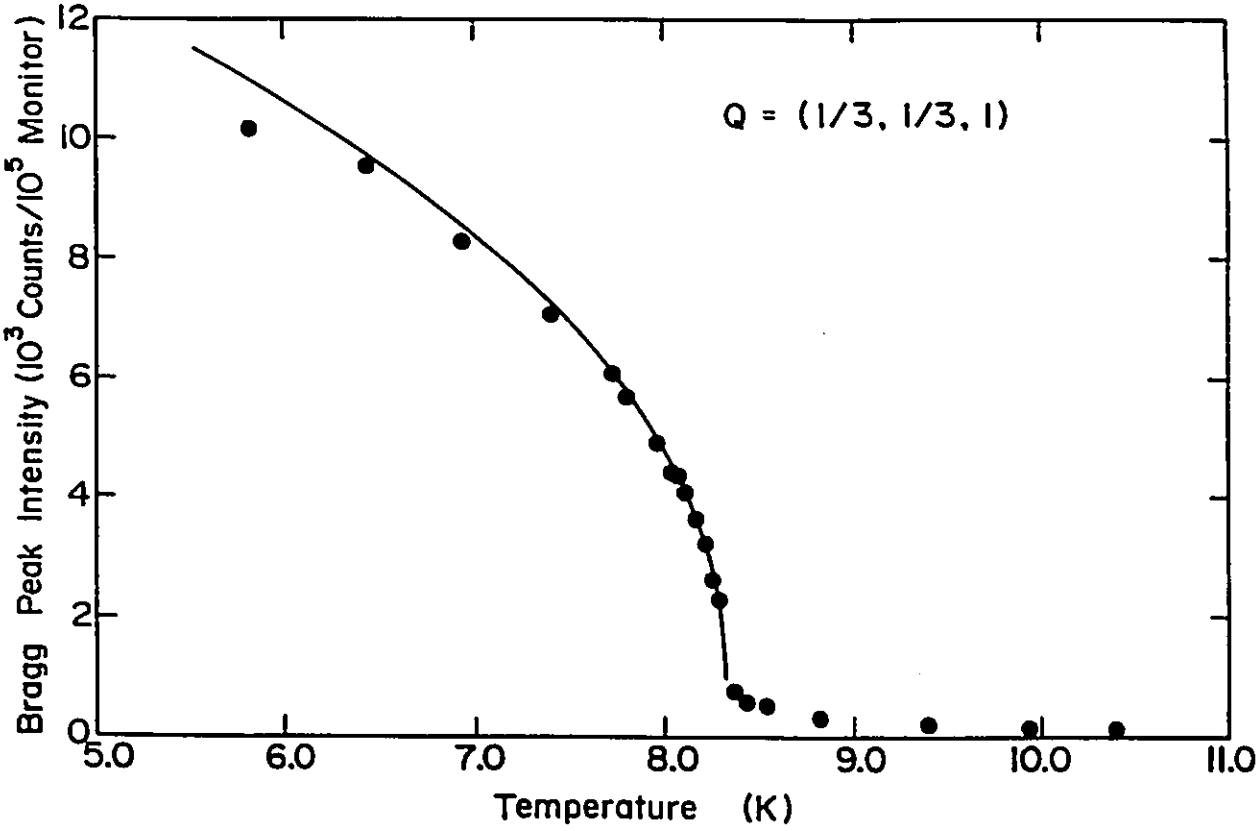

Figure 3.5: Magnetic Bragg peak intensity as a function of temperature for $Q = (\frac{1}{3},\frac{1}{3},1)$. The line is the result of the fit to a power law described in section 3.4.

from the critical scattering shown in Figure 3.4, non-linear least squares fits to the Ornstein-Zernike expression (equation 2.9) times the magnetic form factor for Mn^{+2} (Watson and Freeman 1961) convoluted with the spectrometer resolution function (see equation 2.16) were carried out for all the scans. A linear background term was also included. The resolution function within the scattering plane (horizontal) was determined experimentally from the mesh of scans over the magnetic Bragg peaks at 4.2 K. The vertical resolution was calculated from the spectrometer configuration. Initially a triangular form for the vertical resolution function was used since this allows an analytic integration for the convolution in this direction. The sample was aligned with one of the two crystallites slightly above the scattering plane and the other slightly below. This was accounted for by introducing the estimated offset into the three dimensional resolution function.

The lines in Figure 3.4 are the results of these fits for the three temperatures shown. All the temperatures measured were fitted with comparable success. The non-linear least squares routine used employed the Levenberg-Marquardt method (Press et al 1986) with analytic calculation of the derivatives of the Lorentzian. The integration over the Gaussian horizontal resolution was done using Gauss-Hermite integration (Press et al 1986). In this method the integral over a Gaussian times some function is

replaced by a weighted summation where the intervals of the summation are determined from the zeros of Hermite polynomials (Abramowitz and Stegun 1965):

$$\int_{-\infty}^{\infty} e^{-x^2} f(x)\, dx \cong \sum_{i=1}^{n} w_i f(x_i) \qquad (3.2)$$

This method is accurate provided the number of steps in the summation is as large as the degree of a polynomial needed to approximate the function, f(x), over the range that the Gaussian has appreciable weight. The worst case will therefore be at low temperatures where the Lorentzian is narrowest. The number of steps needed to integrate accurately was determined by calculating the convolution for test cases where the width of the Lorentzian was comparable to the resolution width and comparing to the results of a standard numerical integration method with a tolerance of 10^{-6}. It was found that the Gauss-Hermite integration with ten steps in the ab-plane and twenty steps along the c-axis (due to the narrower peak in that direction) was accurate to about 2% for the worst case (lowest temperature, near the peak). This was the same as the statistical uncertainty in the data and was therefore deemed to be sufficiently accurate for the fitting routine.

In order to determine the importance of the vertical offset, fits were also performed with no offset; one set

with the actual spectrometer resolution and another with a much broader effective resolution to approximate the effects of shifting the crystallites slightly out of the scattering plane. The effect of this on the critical exponents is discussed below. The validity of approximating the vertical resolution as a triangle was tested by fitting the data around $(\frac{1}{3},\frac{1}{3},1)$, with the background and critical scattering from $(\frac{2}{3},\frac{2}{3},1)$ subtracted (as determined from the previous fits), using a Gaussian vertical resolution and a ten step Gauss-Hermite integration. The results were not significantly affected indicating that the triangular approximation was valid. Fits were done in which the backgrounds and peak positions were independent of temperature; allowing them to vary at each temperature did not affect the values of χ and κ_1 extracted from the data.

The data at the lowest temperature (8.45 K) were also fitted to the Fisher and Burford (1967) form for the critical scattering including the exponent η (equation 2.10). Fits done with nonzero values of η were not better than those obtained using the Ornstein-Zernike form (equation 2.9) suggesting that the temperature was too far from T_N to observe any deviations from a Lorentzian.

In order to extract the order parameter (sublattice magnetization) from the magnetic Bragg peak intensities (Figure 3.5) it was necessary to subtract the temperature independent instrumental background and make a small

correction for the critical scattering background near T_N. Measurements made above T_N were used to determine these corrections. The critical scattering correction was made by fitting the data above T_N with a phenomenological polynomial in T which was reflected about T_N. This was then multiplied by an amplitude ratio and added to the temperature independent instrumental background. The amplitude ratio for the critical scattering below T_N was varied between 0 and 1 (there is less critical scattering below T_N due to the lower temperature). The fits for the critical exponent β described below were not sensitive to the value of the amplitude ratio used so 0.5 was used for this correction.

The analysis described above determines the temperature dependence of the square of the order parameter (M_s^2) for three Bragg peaks, the sublattice susceptibility (χ) for two ordering wavevectors, $(\frac{1}{3},\frac{1}{3},1)$ and $(\frac{2}{3},\frac{2}{3},1)$, and the inverse correlation length (κ_1) in two direction (along c and in the ab-plane). The data were least squares fitted (using the same algorithm as above) to power laws in reduced temperature (equation 1.1) with a single value of T_N. This meant that T_N was constrained above by the critical scattering data and below by the order parameter data. Log-log plots of the data and fits for M_s^2, χ, and κ_1 are shown in Figures 3.6, 3.7 and 3.8 respectively. Exponents for the same plot were constrained to be the same. This fit was best for T_N = 8.31 K, β = 0.21, γ = 1.01, and υ = 0.54.

The value of T_N is consistent with that obtained from the magnetic Bragg peak data alone (Mason et al 1987).

Fits were also done in which data sets for each exponent were fitted with independent exponents [ie. three β's from three different Bragg peaks, two γ's from $(\frac{1}{3},\frac{1}{3},1)$ and $(\frac{2}{3},\frac{2}{3},1)$, and two υ's from the c-axis and ab-plane directions]. The resulting exponents differed only slightly from the values given above and the averages were the same. In the case of the magnetic Bragg peak data this indicates that extinction was not a significant effect since it would be manifested quite differently for each peak. The fact that the two values of υ are the same despite the difference in inverse correlation length of about a factor of eight throughout the critical region (see Figure 3.8) is consistent with expectations for a system with anisotropic interactions (Binder and Wang 1989) and indicates that the lineshape analysis has been done correctly.

In order to determine the significance of the approximations for the vertical resolution as discussed above, fits were done using the values of χ and κ_1 obtained from the resolutions with zero vertical offset. In both cases the largest effect was on the exponent γ which varied between 0.95 and 1.05, depending on the vertical resolution. There was a similar effect on υ but it was much smaller.

There was a small variation of the fitted critical exponents with T_N. This is shown in Figure 3.9 where υ and

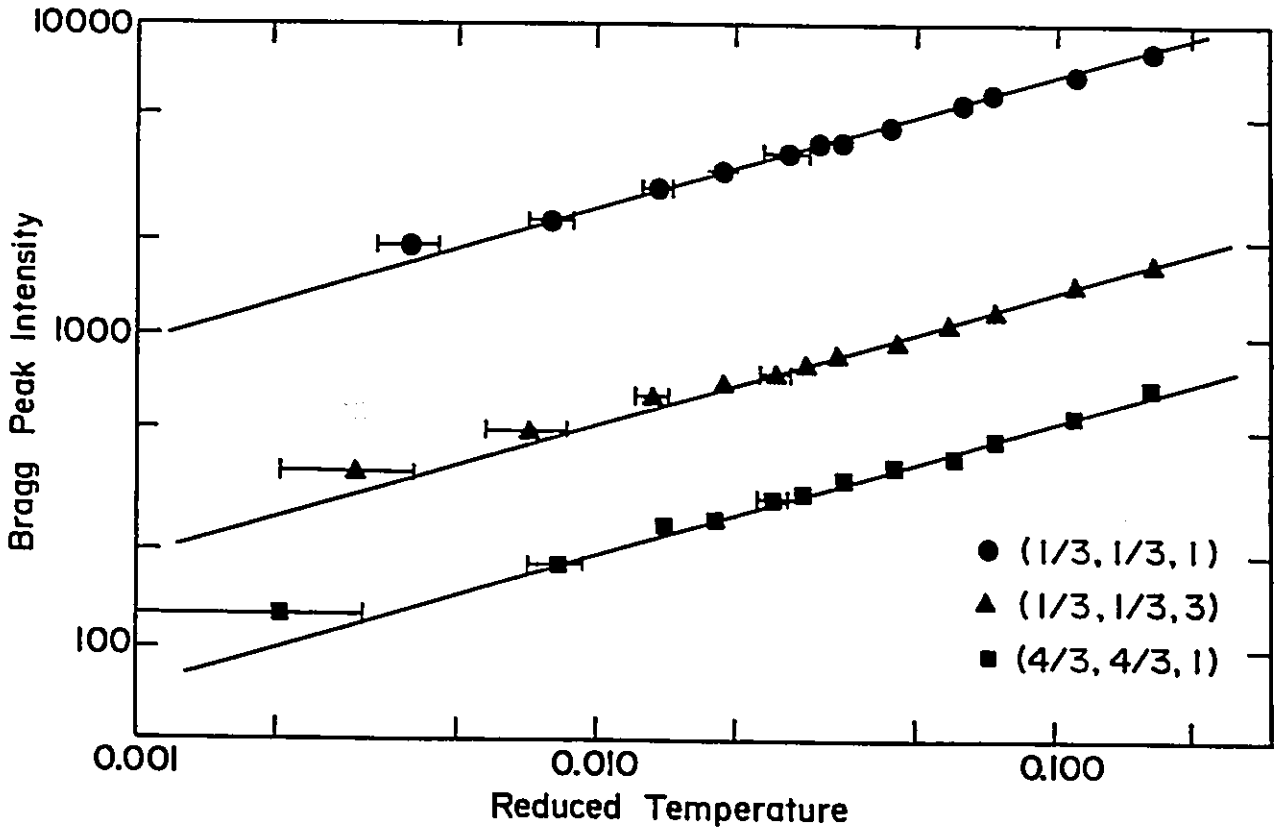

Figure 3.6: Log-log plot of magnetic Bragg peak intensity as a function of reduced temperature for Q = $(\frac{1}{3},\frac{1}{3},1)$, $(\frac{1}{3},\frac{1}{3},3)$, and $(\frac{4}{3},\frac{4}{3},1)$. The lines are the results of fit to a power law in reduced temperature with exponents $\beta = 0.21$.

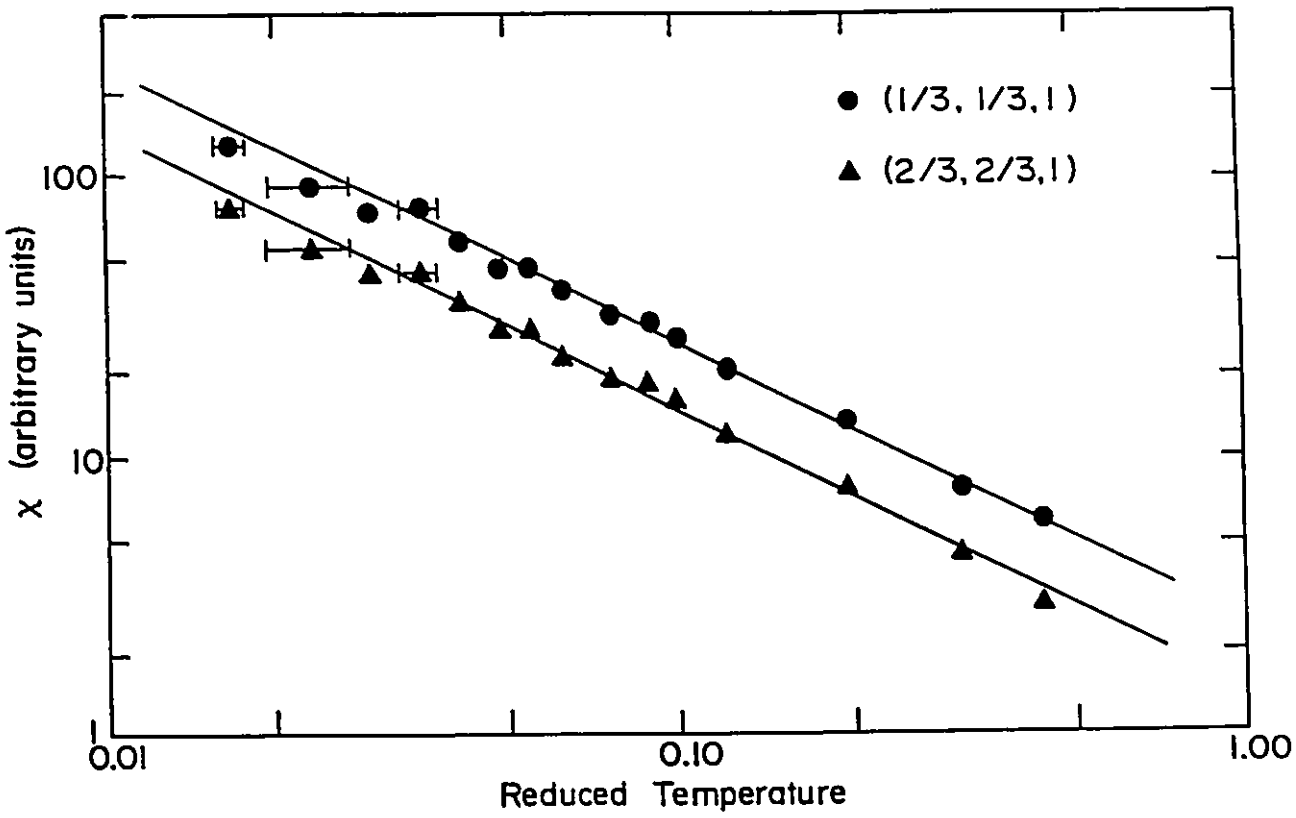

Figure 3.7: Log-log plot of the sublattice susceptibility (χ) as a function of reduced temperature for Q = $(\frac{1}{3},\frac{1}{3},1)$ and $(\frac{2}{3},\frac{2}{3},1)$. The lines are the results of a fit to a power law with exponent $\gamma = 1.01$.

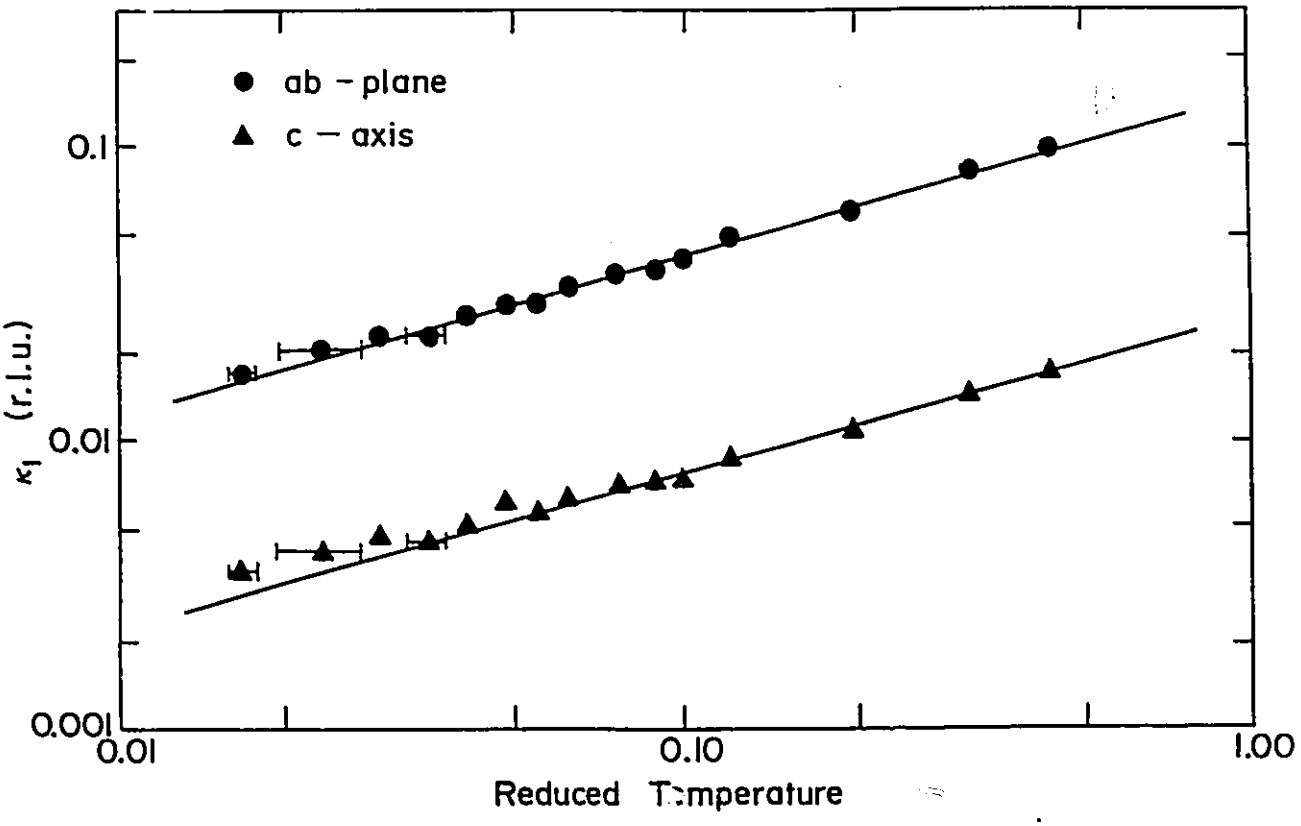

Figure 3.8: Log-log plot of the inverse correlation length (κ_1) as a function of reduced temperature, along the c-axis and in the ab-plane. The lines are the results of a fit to a power law in reduced temperature with exponent $\upsilon = 0.54$.

β have been scaled as indicated. The data in this figure were obtained by constraining the value of T_N and optimizing the exponents. The quality of the fits deteriorated as T_N was changed from the optimum value of 8.31 K and the range of Figure 3.9 indicates the range over which T_N could reasonably extend given the upper and lower bounds presented by the data.

Based on the variation of the critical exponents with T_N, the effects of the vertical resolution and the uncertainty in the least squares fitting procedure it was concluded that $\gamma = 1.01 \pm 0.08$, $\upsilon = 0.54 \pm 0.03$ and $\beta = 0.21 \pm 0.02$ for $CsMnBr_3$. These results have been confirmed by independent neutron scattering measurements (Kadowaki et al 1988 and Ajiro et al 1988).

3.5 Discussion

The static critical exponents for $CsMnBr_3$ (including the specific heat exponent, α (Belanger et al 1990)) are summarized in Table III along with the predictions for the $Z_2 \times S_1$ universality class (Kawamura 1989) and the standard XY model (S_1 universality class) (Baker et al 1978). The experimental values are in good agreement with the predictions for the $Z_2 \times S_1$ universality class. They are not consistent with those for the XY model or with any other standard model in which the universality class is determined by the dimensionality of the order parameter.

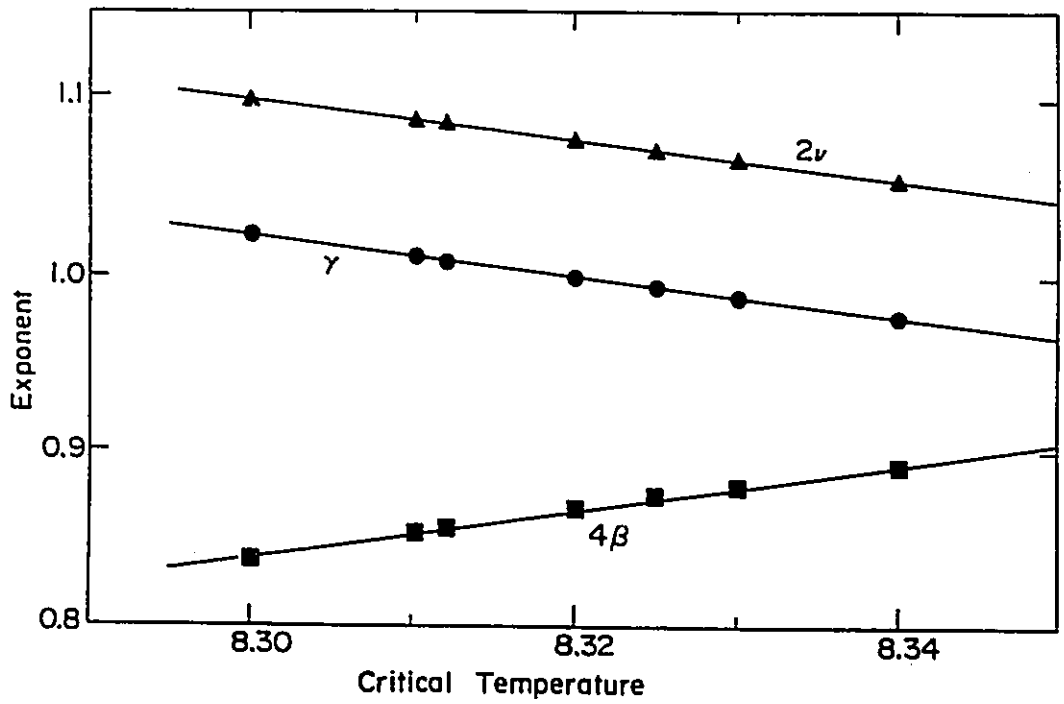

Figure 3.9: Variation of the fitted critical exponents with the critical temperature, T_N(K). The best fit was obtained with T_N = 8.31 K. υ and β have been scaled by 2 and 4 respectively for clarity.

Exponent	$Z_2 \times S_1$	S_1	$CsMnBr_3$
γ	1.1 ± 0.1	1.316 ± 0.009	1.01 ± 0.08
υ	0.53 ± 0.03	0.669 ± 0.007	0.54 ± 0.03
β	0.25 ± 0.02	0.345 ± 0.011	0.21 ± 0.02
α	0.40 ± 0.04	-0.01	0.35 ± 0.05

Table III: Critical exponents γ, υ, β, and α for the $Z_2 \times S_1$ universality class (Kawamura 1989), the standard XY model (S_1) (Baker et al 1978), and $CsMnBr_3$. The experimental values for γ, υ, and β are from the present work. The experimental value for α is from the specific heat measurement of Belanger et al (1990).

The critical exponents for $CsMnBr_3$ are quite similar to those measured for VCl_2 (see Table II), a Heisenberg triangular antiferromagnet belonging to the SO(3) universality class. The additional degeneracy brought about by the lattice frustration has a larger effect on the critical properties than the dimensionality of the order parameter. In the case of VCl_2 the measured critical failed to satisfy the hyperscaling relation (equation 1.8) between γ, υ, and β by 2.6 standard errors. Failure to follow hyperscaling indicates that there is not a single length scale at the critical point (Binder and Wang 1989), possibly due to different characteristic lengths for the chiral and spin wave fluctuations. The exponents for $CsMnBr_3$ fail to satisfy equation 1.8 by 1.5 standard errors. Exponents fitted with a slightly higher T_N (see Figure 3.9) are closer to satisfying hyperscaling although the critical

temperature necessary for exact agreement (8.50 K) is clearly too high.

There is also a hyperscaling relation between υ and α (Collins 1989):

$$2 - \alpha = d\upsilon \tag{3.3}$$

For $\upsilon = 0.54 \pm 0.03$ one obtains a value for α of 0.38 ± 0.09 which is in good agreement with both the theoretical prediction (Kawamura 1989) and the measured exponent (Belanger et al 1990). This agreement, together with the somewhat poorer agreement with equation 1.8, suggests that the critical phase transition in $CsMnBr_3$ is not inconsistent with hyperscaling.

γ and υ can be used to determine the critical exponent η from a scaling law (Collins 1989):

$$\gamma = 2\upsilon(1-\eta/2), \tag{3.3}$$

resulting in a value of 0.13. This is surprisingly large for a three dimensional system (η is usually $\cong$ 0.04 for d = 3). However, the uncertainty is also large (0.18) and includes the range of expected values for η. Whether a large value of η is a characteristic of ordering with a chiral degeneracy could be resolved by careful lineshape measurements closer to T_N with a better quality crystal.

CHAPTER 4

MAGNETIC PHASE DIAGRAM AND SUSCEPTIBILITY OF $CsMnBr_3$

4.1 Introduction

The 120° magnetic structure that forms the ground state for $CsMnBr_3$, in the absence of an applied magnetic field, arises from a balance of competing interactions, a consequence of the lattice frustration. The additional term in the Hamiltonian (equation 1.16) that would arise due the the application of a magnetic field in the ab-plane might therefore be expected to change the balance resulting in additional magnetic phases. Measurements of the temperature dependence of the magnetic Bragg peak intensity in a 3.7 T magnetic field applied along the (100) direction have shown a splitting of the zero field transition (Gaulin et al 1987). The nature of the intermediate phase and the the phase diagram were not determined.

Minimization of the spin configuration energy at zero temperature taking into account quantum renormalization of the spin $\frac{5}{2}$ moments has predicted a transition from a six sublattice triangular phase to a four sublattice phase without any chirality at 6.1 T and zero temperature (Chubukov 1988). Non-local Landau theory has been applied to the general problem of the magnetic phase diagrams of

uniaxial and planar antiferromagnets in hexagonal crystals (Plumer et al 1989). For the planar case appropriate to $CsMnBr_3$, a tetracritical point is predicted for $T = T_N$, $H = 0$. An infinitesimal magnetic field will split the zero field transition. Novel multicritical points may also occur at non-zero magnetic fields depending on the anisotropies present in the system.

This chapter presents a determination of the magnetic phase diagram of $CsMnBr_3$ by elastic neutron scattering and susceptibility measurements near the tetracritical point. The phase diagram measurements were performed on the H5 triple-axis spectrometer at the Brookhaven National Laboratory. The spectrometer was operated in the elastic mode using the (002) reflection of vertically focussed pyrolytic graphite to monochromate and analyze the neutrons. The measurements were done using a neutron energy of 3.3 THz with a pyrolytic graphite filter in the incident beam to remove higher order contamination. Collimation before and after the sample was 20′.

The crystal was the same one used in the critical scattering measurements that were described in Chapter 3. It was mounted in an aluminum sample can filled with He gas to insure good thermal contact. The can was mounted in a cryostat with the $(\xi\xi\zeta)$ plane of the crystal was horizontal. The temperature was monitored using a carbon glass resistor (this sensor is highly insensitive to the presence of a

magnetic field). The temperature stability was better than 20 mK for 7 K < T < 10 K, and better than 10 mK below 7 K. A split coil superconducting magnet with the field direction perpendicular to the scattering plane was used to apply magnetic fields of up to 6.5 T in the (100) direction.

The measurements described in this chapter have been published in the scientific literature (Gaulin et al 1989b and Mason et al 1990a).

4.1 Magnetic Phase Boundaries

In addition to being proportional to the square of the intensity of the sublattice magnetization, the magnetic Bragg peak cross section (equation 2.12) also depends on the magnetic structure as does the polarization prefactor in equation 2.4. The intensity of the $(\frac{1}{3},\frac{1}{3},1)$ and $(\frac{2}{3},\frac{2}{3},1)$ magnetic Bragg peaks as a function of temperature in an applied magnetic field of 4.2 T is shown in Figure 4.1. There is a critical phase transition from the paramagnetic state to an an antiferromagnetic state at $T_{II} = 9.00 \pm 0.10$ K. In contrast to the smooth temperature evolution of the order parameter in zero field (see Figure 3.5) there is a distinct kink in the intensity at $T_I = 7.15 \pm 0.10$ K indicating a critical phase transition between two different ordered states. The fact that the Bragg peaks of the two structures occur at the same points in reciprocal space (no new magnetic Bragg peaks were observed) indicates

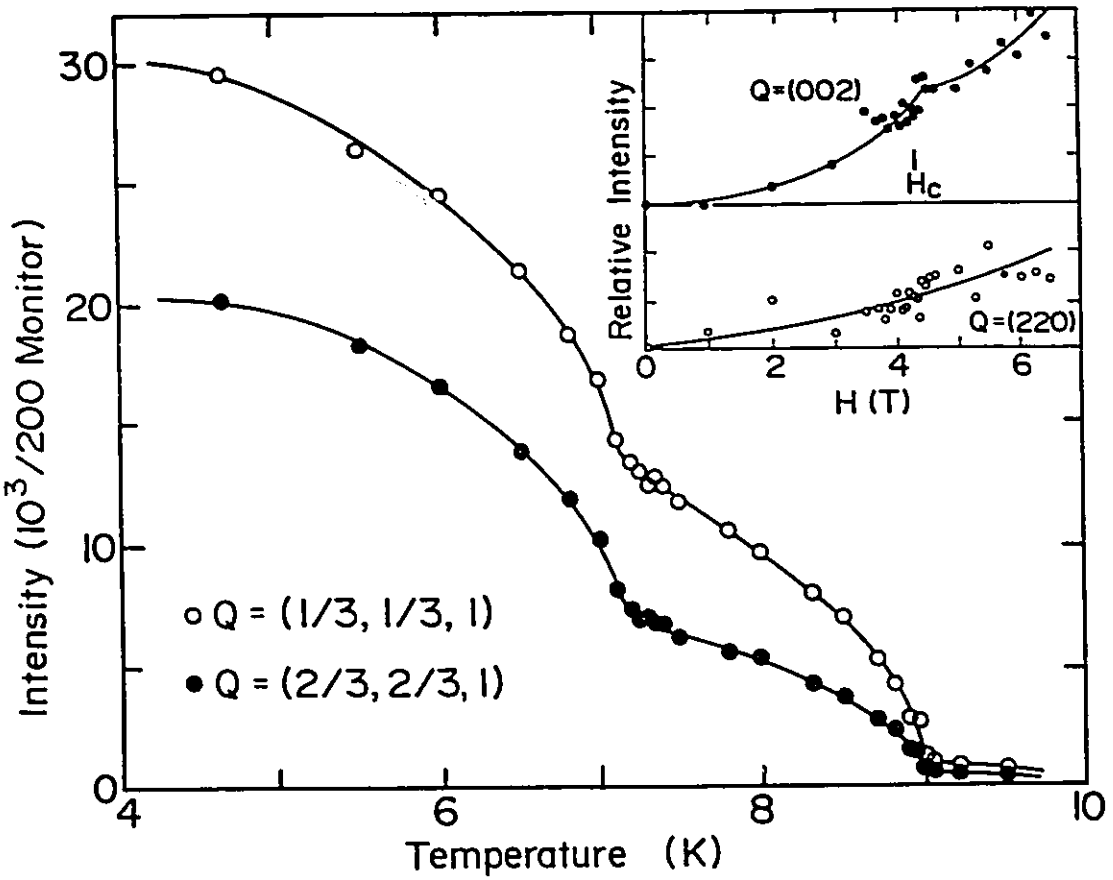

Figure 4.1: Temperature dependence of the antiferromagnetic Bragg peak intensity for the $(\frac{1}{3},\frac{1}{3},1)$ and $(\frac{2}{3},\frac{2}{3},1)$ reflections in an applied field of 4.2 T. Successive phase transitions from the paramagnetic phase to the spin-flop phase and from the spin-flop phase to the triangular phase occur at T_{II} = 9.00 ± 0.10 K and T_I = 7.15 ± 0.10 K respectively. The inset shows the field dependence of the (002) and (220) reflections for T = 7.0 K, indicating the increasing ferromagnetic component with increasing applied field.

that the two structures have the same unit cell. The change in intensity reflects the fact that the spin orientations in the two phases are different.

The inset in Figure 4.1 shows the field dependence of the intensity of the (220) and (002) reflections for T = 7.0 K. These are reflections of the nuclear lattice of $CsMnBr_3$ and are therefore sensitive to the ferromagnetically aligned component of spin. There is a gradual increase of the ferromagnetic moment with increasing field. There is a suggestion of a kink in the (002) data at the critical field although the statistics are rather poor due to the large nuclear component in the intensity.

Similar scans to the data of Figure 4.1, for various applied magnetic fields, have been used to map out the phase boundaries for the two phase transitions. At low temperatures, scans of the intensity as a function of field for fixed temperature were used to provided the sharpest signature of the transition between the two ordered phases. The resulting phase diagram is shown in Figure 4.2. The triangle plotted on the T = 0 K line indicates the predicted critical field of 6.1 T (Chubukov 1988). There is good agreement between this prediction and the extrapolation of the finite temperature experimental data ($H_c \cong 6.2$ T).

It is not possible to determine uniquely the magnetic structure for this noncollinear system from the measurements of four Bragg peak intensities; however, it is

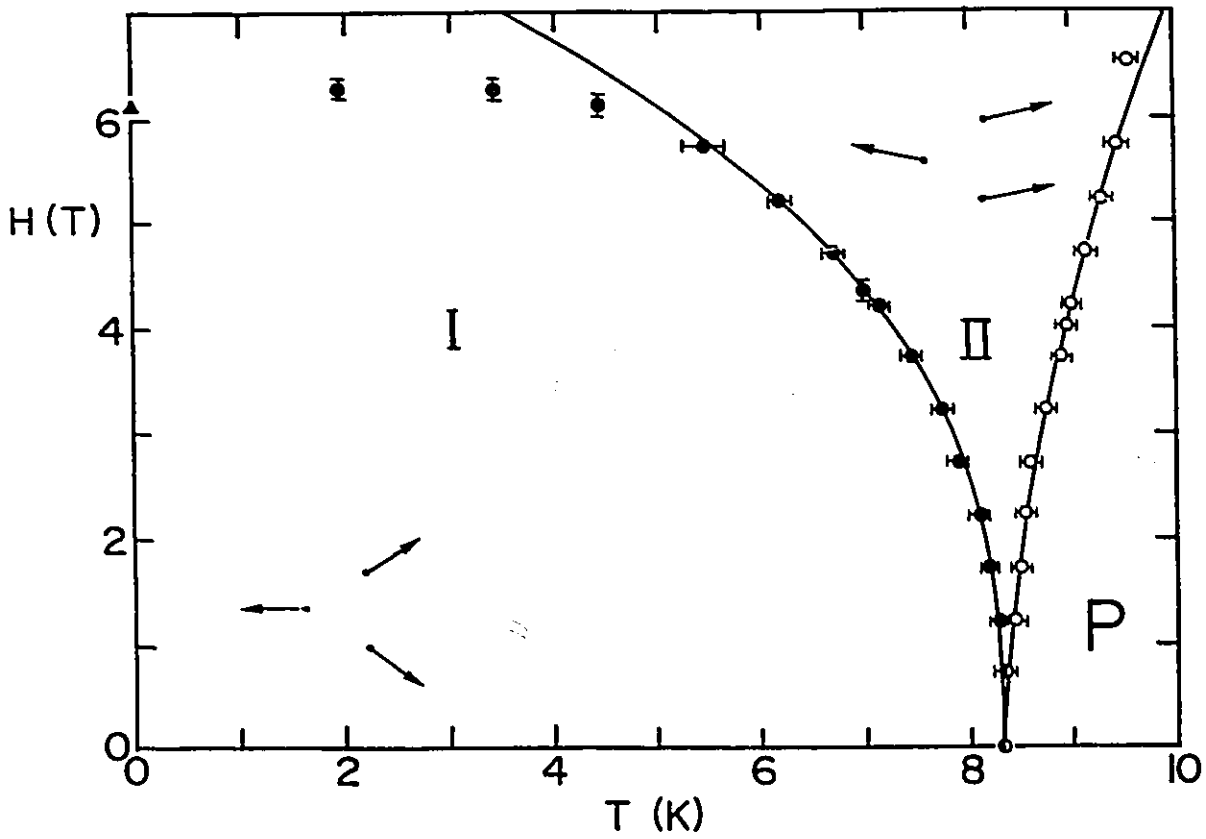

Figure 4.2: The magnetic phase diagram of $CsMnBr_3$ for a field applied along the (100) direction. P denotes the paramagnetic phase, I , the spin flop phase, and II the triangular phase. The spin configurations for a triad of nearest neighbour spins is shown for each ordered phase. The lines are the results of least squares fits to power laws near the tetracritical point (see section 4.3).

possible to test the consistency with the structure predicted by Chubukov (1988). The intensities for the peaks measured [$(\frac{1}{3},\frac{1}{3},1)$, $(\frac{2}{3},\frac{2}{3},1)$, $(\frac{4}{3},\frac{4}{3},1)$, and $(\frac{1}{3},\frac{1}{3},3)$] together with the field dependence of the ferromagnetic component are consistent with the structures predicted on the basis of the microscopic Hamiltonian (Chubukov 1988).

The low field, low temperature, phase (I) is a distortion of the triangular structure with a small cant of the moments towards the magnetic field and a larger component perpendicular to the field direction that alternates antiferromagnetically from layer to layer. Both the cant and the alternating perpendicular component increase with increasing magnetic field. At the transition between phase I and II, two of the sublattices collapse together resulting in a phase that has no chirality. As the field is increased in phase II all the spins gradually cant towards the magnetic field direction. These magnetic structures are shown schematically for a triad of spins in the basal plane in Figure 4.2 for a magnetic field applied along the positive y axis of the graph. The Monte Carlo simulations described in Chapter 5 confirm these spin structures.

All the data suggest that the phase transitions are continuous (ie. critical phase transitions) over the range of temperatures and fields measured. Temperature scans were carried out with both increasing and decreasing temperature

and no evidence of hysteresis (which is usually found for first order phase transitions) was observed. The phase diagram shown in Figure 4.2 indicates that the $T = T_N$, $H = 0$ transition is a tetracritical point.

4.3 Crossover Exponents and Susceptibility

The lines in Figure 4.2 are the results of a least squares fit of the critical temperatures as a function of applied field to the functional form predicted to hold near the tetracritical point for tetragonal XY antiferromagnets (Kerszberg and Mukamel 1978):

$$\frac{T_i(H^2) - T_N}{T_N} \propto (H^2)^{1/\psi_i} . \qquad (4.1)$$

The fits give crossover exponents $\psi_{P\text{-}II} = 1.21 \pm 0.07$ and $\psi_{II\text{-}I} = 0.75 \pm 0.05$. The renormalization group prediction for $CsMnBr_3$ is that $\psi_{P\text{-}II} = \psi_{II\text{-}I} = \phi \cong 1.04$ (Kawamura et al 1990). The fact that both phase boundary lines are scaled by a single crossover exponent near the tetracritical point is a unique feature of the chiral fixed point in the renormalization group analysis. The disagreement between the experiment and the theoretical prediction could be due to the potentially significant nonuniversal corrections to power law behaviour (Kawamura et al 1990) making a precise determination of the ψ's difficult. The data for the

critical temperatures was not sufficiently precise to warrant the inclusion of the leading order corrections in the fitting procedure. It is also possible that the discrepancy between the theory and experiment is due to another unstable fixed point in the vicinity of the chiral one which may determine the behaviour of the phase boundaries away from the tetracritical point.

The scaling analysis of the tetracritical point in $CsMnBr_3$ (Kawamura et al 1990) predicts that the zero field uniform magnetic susceptibility (χ) should exhibit singular behaviour at T_N of the form:

$$\chi \alpha |t|^{-\tilde{\gamma}} \qquad (4.2)$$

where $\tilde{\gamma} \equiv -(2-\alpha-\phi)$. Since α has been measured (Belanger et al 1990) it is possible to determine the value of ϕ by finding $\tilde{\gamma}$. For $\phi < 2-\alpha$ (≈ 1.65) $\tilde{\gamma}$ is less than zero so the singularity would be in the form of a cusp, with χ approaching zero as T tends towards T_N. Measurement of $\tilde{\gamma}$ would give an indication of whether the disagreement between ϕ and the measured ψ's is due to difficulties in the analysis or a deficiency of the theory. Previous measurements of the temperature dependence of the magnetic susceptibility (Eibshutz et al 1973) did not have sufficient data near T_N to address this point. In addition the value of the applied field used to measure the susceptibility was

rather large (15 300 Oe). For a field this large applied perpendicular to the c axis the phase transitions are split by 0.21 K.

The zero field uniform susceptibility of $CsMnBr_3$ was measured using a Quantum Design squid magnetometer in the vicinity of T_N. Two crystals cut from the same piece as the crystal used in the neutron scattering measurements were used to determine the susceptibility for a magnetic field applied parallel and perpendicular to the c-axis. The results are shown in Figures 4.3 and 4.4 respectively for an applied field of 500 Oe. In both cases the temperature dependence of χ is monotonic near T_N although the phase transition is marked by a change in slope. The measurements have been performed for magnetic fields of 1000, 500, and 100 Oe and the results are the same for all three fields. The consistency of the results for the different values of the applied field indicates that the results are representative of the zero field susceptibility. Calculating the splitting of the two phase transitions for a 500 Oe field applied perpendicular to the c axis based on the cross over exponents one obtains 0.0004 K, indicating how close this field is to the tetracritical point. The size of the temperature steps was 0.02 K so any singularity in χ would have to be measurable only for $|t| < 10^{-3}$. This seems unlikely since the critical scattering results showed that the critical regime extended up to reduced temperatures

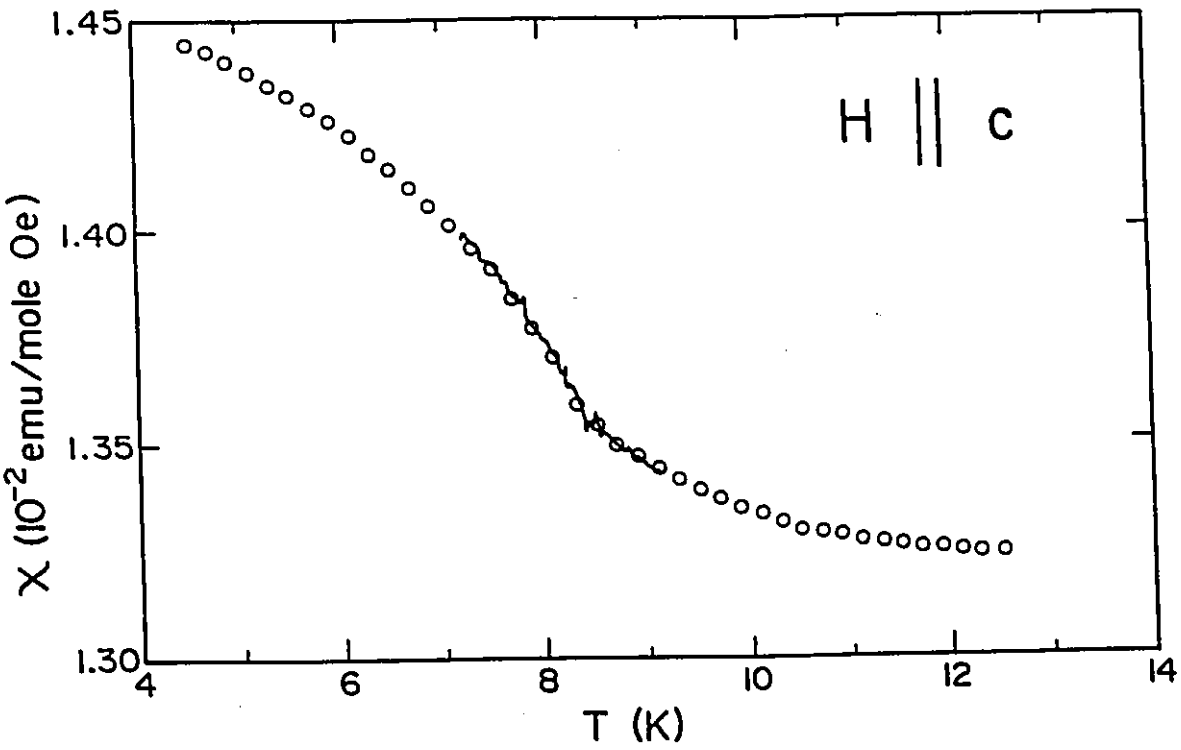

Figure 4.3: Uniform magnetic susceptibility for a magnetic field (500 Oe) applied parallel to the c-axis. The line shows the data for a 100 Oe field

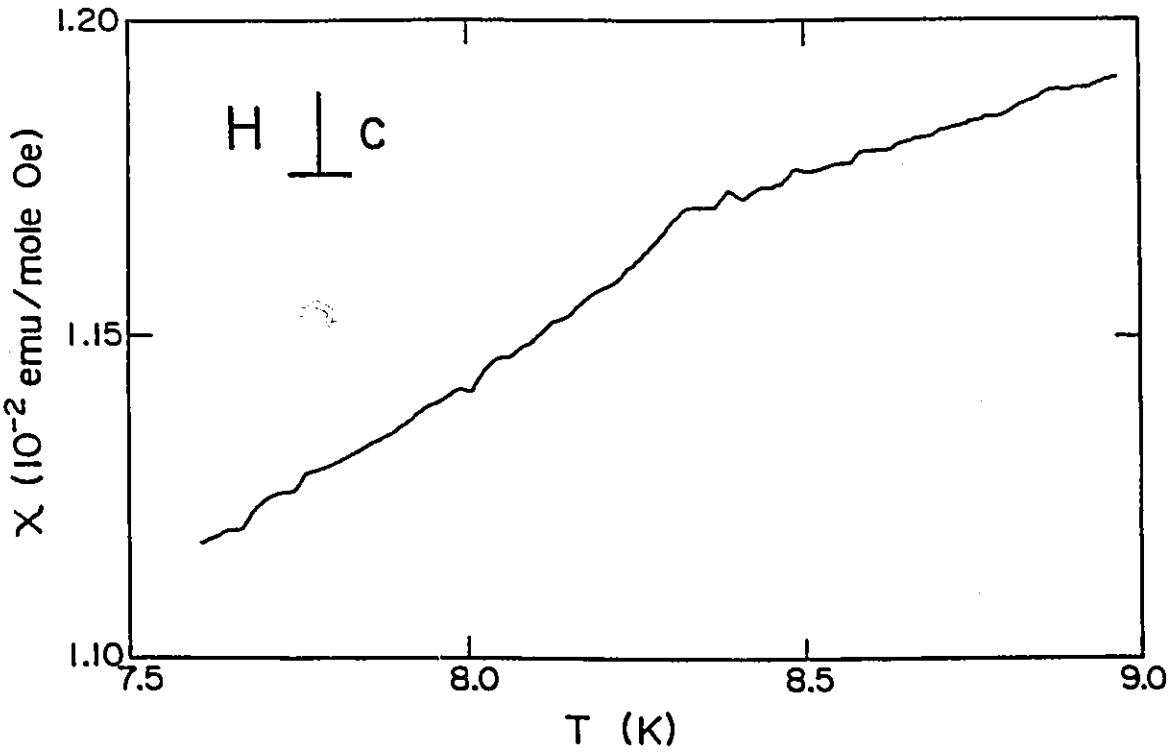

Figure 4.4: Uniform magnetic susceptibility for a magnetic field (500 Oe) applied perpendicular to the c-axis.

greater than 10^{-1}. There is no evidence that the susceptibility exhibits a singularity at the tetracritical point.

The phase transition is more clearly evident in the derivative of the susceptibility with respect to temperature ($d\chi/dT$) shown in Figure 4.5 for the two field directions. The derivative was calculated by taking a weighted average of the $\Delta\chi/\Delta T$'s near a point in order to reduce the scatter due to fluctuations in the measured susceptibility. In both cases $d\chi/dT$ is independent of temperature above T_N and exhibits a sharp discontinuity at the tetracritical point. For H parallel to c there is a downturn in $d\chi/dT$ as T_N is approached from below while for H perpendicular to c there is an upturn.

The temperature dependence of the magnetic Bragg peak intensity can be used to determine the critical exponent β as described in Chapter 3. Data from the $(\frac{1}{3},\frac{1}{3},1)$ and $(\frac{2}{3},\frac{2}{3},1)$ reflections for H = 0 and H = 4.0 T were least squares fitted to a power law in reduced temperature resulting in $\beta = 0.24 \pm 0.02$ for H = 0 and $\beta = 0.29 \pm 0.02$ for H = 4.0 T (spin-flop phase). The results for the $(\frac{1}{3},\frac{1}{3},1)$ reflection are shown in Figure 4.6. The previous determination of β in the absence of a magnetic field showed no extinction effects so these measurements on the same crystal should also be free from errors due to extinction. This is confirmed by the fact that there were no systematic

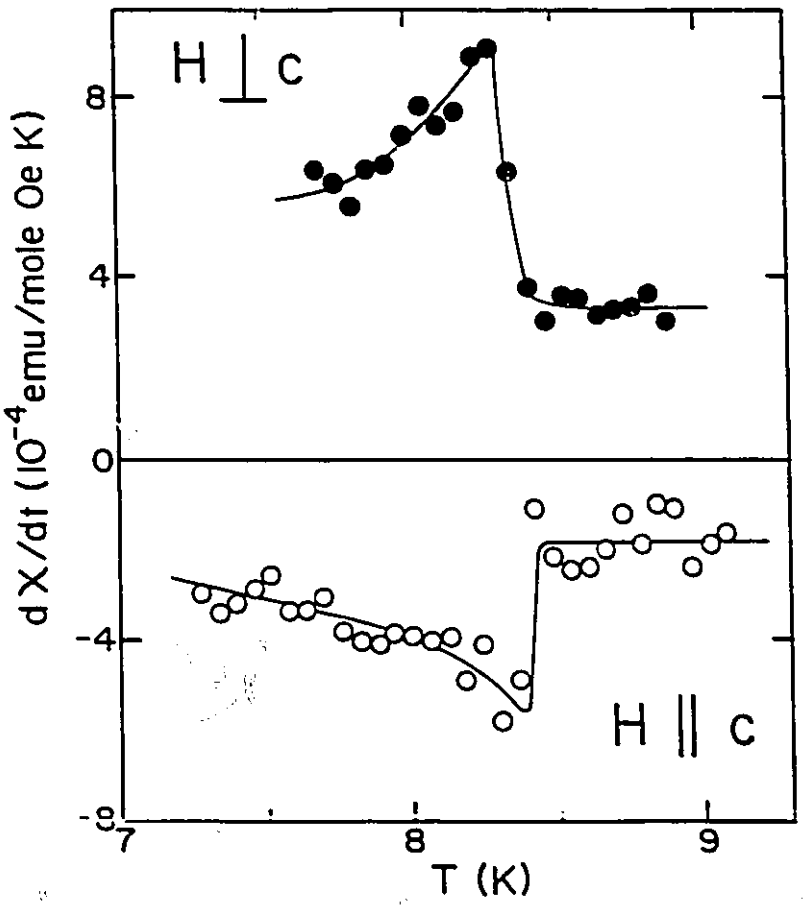

Figure 4.5: Derivative of the susceptibility with respect to temperature ($d\chi/dT$) for a magnetic field parallel and perpendicular to the c axis.

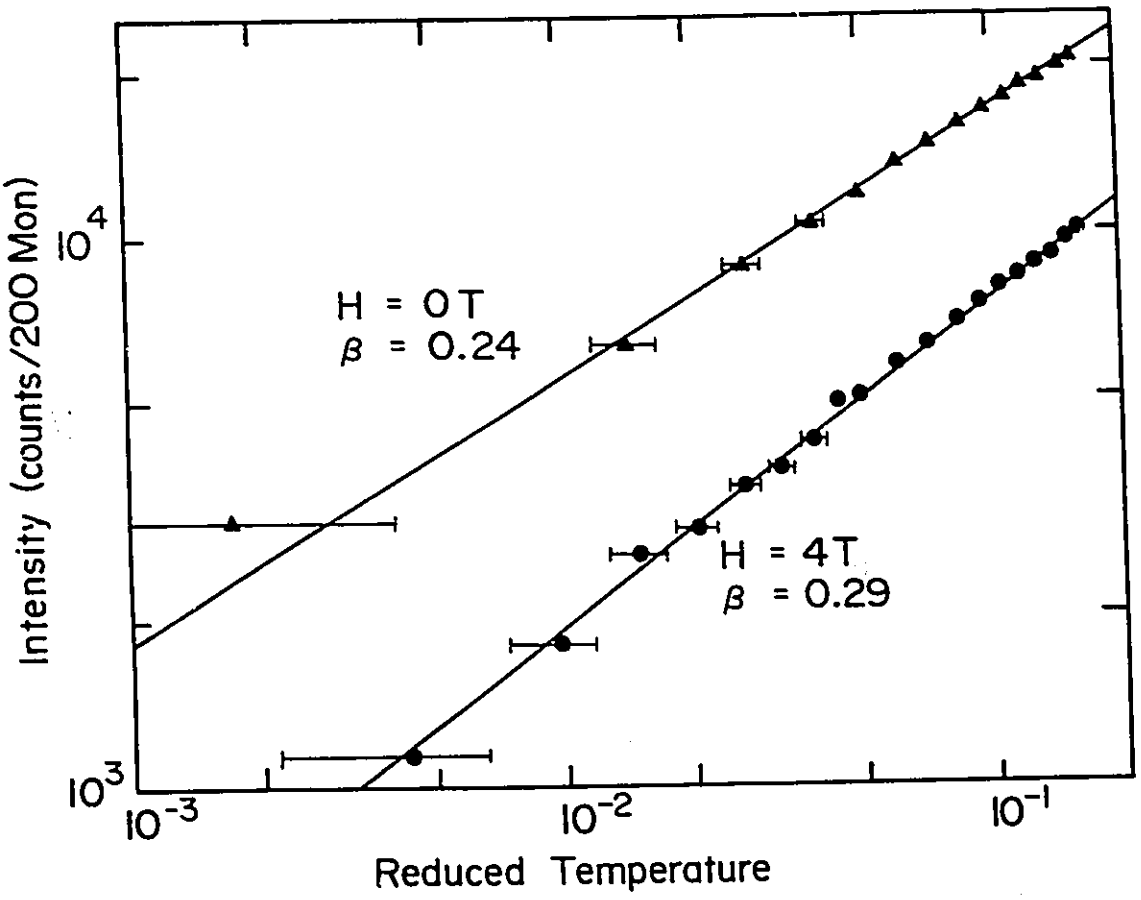

Figure 4.6: Log-log plot of the $(\frac{1}{3},\frac{1}{3},1)$ magnetic Bragg peak intensity as a function of reduced temperature for H = 0 T and H = 4 T. The lines are the results of fits to power laws with the β values indicated in the Figure.

differences observed for the two Bragg peaks measured.

4.4 Discussion

The results of the determination of the magnetic phase diagram of $CsMnBr_3$ for a field applied along the (100) direction indicate that in addition to possessing unusual static critical exponents, the zero field phase transition is a tetracritical point. This raises the question of whether or not the multicriticality of the zero field phase transition is sufficient to explain the nonuniversal static critical exponents. This is not a question that can be addressed experimentally but the renormalization group analysis (Kawamura 1988) indicates the fixed point for this phase transition is a unique one and the tetracriticality is one of its properties. For this reason a determination of the magnetic phase diagram of other triangular antiferromagnets, such as VCl_2 would be of considerable interest. Holmium metal which has a spiral spin structure and is predicted to belong to the $Z_2 \times S_1$ universality class (Kawamura 1988) appears to have a similar magnetic phase diagram (Steinitz et al 1987).

The magnetic phase diagram shown in Figure 4.2 has several other interesting features. The critical temperature for the paramagnetic to spin flop phase transition increases with increasing magnetic field. This is in contrast to the decrease usually observed for

antiferromagnets in a magnetic field. The phase transition from phase I to phase II involves an increase in the component of the spins perpendicular to the field much like what occurs in uniaxial antiferromagnets with a bicritical point (Shapira and Foner 1970) but, unlike the uniaxial antiferromagnets, the phase transition is continuous.

The behaviour of the phase boundaries near the tetracritical point follows a power law with crossover exponents $\psi_{P\text{-}II} = 1.21 \pm 0.07$ and $\psi_{II\text{-}I} = 0.75 \pm 0.05$. The fact that both are less than 2 means they cross the H = 0 T line at an angle of 90° and the range of stability of phase II vanishes like a power law. This is qualitatively different from other tetracritical points observed in stressed $LaAlO_3$ (Muller et al 1983) and $GdAlO_3$ in a magnetic field (Rohrer and Gerber 1977). It is more like the tetracritical point predicted (Kerszberg and Mukamel 1978) but not observed for the tetragonal XY antiferromagnet, Fe_2As, in a magnetic field (Corliss et al 1982).

The fact that the magnetic phase boundaries do not scale with a single crossover exponent, $\phi \cong 1.04$, near the tetracritical point could reflect a nonuniversal correction to power law behaviour or a lack of sufficiently precise data for low values of the magnetic field. The failure to observe a singularity in the zero field uniform susceptibility suggests that the origin of the discrepancy may lie in the theory. Although the qualitative features of

the magnetic phase diagram can be understood in the context of nonlocal Landau theory (Plumer and Caillé 1990) a detailed quantitative understanding, based on the microscopic Hamiltonian (equation 1.16) poses a significant challenge to theory.

The value for the order parameter critical exponent, β, in the absence of an applied field was found to be 0.24 $\pm$ 0.02 in good agreement with the more careful measurement of Chapter 3. In an applied field of 4.0 T the phase transition from the paramagnetic state in phase II had a value of β = 0.29 $\pm$ 0.02. This is significantly larger than the zero field β and is quite close to that expected for the three dimensional Ising model (0.31). The application of a magnetic field within the basal plane has two effects. It breaks the XY symmetry within the plane and destroys the chiral degree of freedom (in phase II there is no chirality). This would lead one to conclude that three dimensional Ising behaviour is to be expected for the P-II phase transition, however, the structure maps onto a six state clock model which should exhibit XY like critical exponents (Kawamura et al 1990). The value of β for the XY model is 0.345 $\pm$ 0.011 (Baker et al 1978) which is clearly not consistent with the measured value for $CsMnBr_3$ in a 4.0 T magnetic field. This discrepancy could be due to the cross over from $Z_2 \times S_1$ to XY critical behaviour not being complete for H = 4.0 T. A measurement of β in a larger

applied field could resolve this point. Whether the universality class of phase II is three dimensional Ising or XY it is clearly within the range of the standard models. β in this phase is definitely higher than for the chiral universality classes.

CHAPTER 5

MONTE CARLO SIMULATIONS

1.1 Introduction

Although the qualitative features of the magnetic phase diagram of $CsMnBr_3$ can be reproduced using Landau theory (Plumer and Caillé 1990) this is a non local formulation and treats the expansion terms in the free energy as parameters that are fit to the data. It would therefore be interesting to see if the magnetic phase diagram described in chapter 4 can be understood on the basis of the magnetic Hamiltonian derived from spin wave measurements (equation 1.16) (Gaulin et al 1987, Falk et al 1987). Magnetic phase diagrams are often sensitive to the presence of additional, smaller terms in the Hamiltonian that may not be sufficiently large to be manifested in the spin wave measurements. This raises the question of whether the tetracriticality of the zero field phase transition is inherent in the simple XY triangular antiferromagnet Hamiltonian or a consequence of additional, unknown, small terms.

Monte Carlo simulation is a numerical method that allows the behaviour of a particular Hamiltonian to be studied (Binder and Heerman 1988). A computer is used to

construct a small model lattice of spins with a random configuration. In the Metropolis algorithm (Metropolis et al 1953) a series of configurations of the model lattice are generated by changing the orientation of a single site randomly and accepting the new configuration if a randomly generated number between zero and one is less than the Boltzmann factor, $\exp(-\delta\mathcal{H}/k_B T)$, for the change in energy, $\delta\mathcal{H}$, calculated from the Hamiltonian being simulated. Iteration of this proceedure results, after sufficient steps to equilibrate the system, in a series of configurations which may be used to calculate ensemble averages of the quantities of interest such as the internal energy, $<U>$, or the sublattice magnetization, $<M_s>$. The fluctuations in these quantities can be used to determine the specific heat, $<C_H>$, and the sublattice susceptibility, $<\chi_s>$. For a sufficiently large number of steps the averages will approach the expectation values for the finite system being simulated. Since the model system is generally quite small it may be necessary to simulate different sized lattices in order to determine the importance of finite size effects and estimate the behaviour for the infinite system.

This chapter describes Monte Carlo simulations of the magnetic Hamiltonian of $CsMnBr_3$ as a function of temperature and applied magnetic field. The results have been published in the scientific literature (Mason et al 1990b). The critical behaviour of the XY triangular

antiferromagnet in the absence of a magnetic field has been the subject of extensive Monte Carlo simulations (Kawamura 1988a, 1989) and it was in this context that the unusual critical properties of the system were first discussed. Further details regarding the Monte Carlo method in general may be found in Binder and Heerman (1988).

1.2 Monte Carlo Simulations of $CsMnBr_3$

Classical, zero temperature calculations have shown that provided the planar anisotropy $D > 3J_{ab}$ (see equation 1.16) the spins remain confined to the ab plane upon application of a magnetic field within the plane (Chubukov 1988). This is the case for $CsMnBr_3$ and no canting out of the planes was observed in the neutron scattering measurements described in chapter 4. Since the spins remain in the basal plane for the region of parameter space of interest ($H \perp c$ and $T < 15$ K) Monte Carlo simulations have been performed for the computationally more tractable case of XY spins on a triangular lattice with nearest neighbour antiferromagnetic interactions:

$$\mathcal{H} = -2J_c \sum_{i>j} \mathbf{S}_i \cdot \mathbf{S}_j - 2J_{ab} \sum_{i>j} \mathbf{S}_i \cdot \mathbf{S}_j - H \sum_i S_i^x \qquad (5.1)$$

This Hamiltonian differs from (1.16) because the spins are now two dimensional vectors and a magnetic field, H, in the

x direction has been explicitly included. It is simpler to carry out computations in dimensionless units so J_{ab} and the length of the spin vector have been set equal to one. All other variables are scaled relative to these (eg. $J_c = 463$) so as to allow conversion back to standard units by inserting the appropriate values for S and J_{ab}. The dimensionless temperature, T, is therefore related to the temperature in Kelvin by:

$$T = \frac{k_B T(K)}{2J_{ab}S^2} . \qquad (5.2)$$

The Mn^{+2} ions are spin $\frac{5}{2}$ so the use of classical spin vectors should not introduce substantial errors. To lowest order, quantum corrections are taken into account through the use of parameters from spin wave measurements which result from fitting the dispersion to classical spin wave theory. The resulting J's are therefore effective exchange interactions that are renormalized from the actual ones for the quantum mechanical system.

Because of the quasi-one-dimensional nature of the Hamiltonian it was necessary to employ a special algorithm for generating new spin configurations in order to avoid extremely long equilibration times. Two types of updating methods were employed alternately. On the first sweep through the lattice an attempt was made to rotate each spin

independently. On every second sweep through the lattice all the spins in each of the highly correlated chains along the c axis were rotated by the same amount. In both cases the total energy change for a new orientation of a spin or chain of spins was used in the Boltzmann factor that determined the success of the new configuration. In this way detailed balance was maintained. This technique is similar to a cluster updating method (Niedermayer 1988) in which a well-correlated region of spins is determined according to some criteria and then rotated by some global amount. The difference in this case is that the a priori knowledge that the chains are well correlated throughout the three dimensional critical region has been used to predetermine the cluster. It is not possible to extend the cluster to more than one chain due to the frustration of the in-plane interactions. The ranges of both the single site and the chain rotations were tuned to provide a 50% acceptance rate for new configurations. The one to one ratio of single site to chain rotations was employed because the number of Monte Carlo steps (MCS) required to reach equilibration was dominated by the number of chain rotations.

Simulations consisting of 5000 - 10000 MCS per spin for equilibration followed by 16000 MCS per spin to calculate ensemble averages, were carried out for a variety of random number sequences and starting configurations for

12 × 12 × 12 lattices with periodic boundary conditions. The simulations were run on Sun workstations using code written in FORTRAN 77. The initial configurations were first brought to equilibrium in zero field by ramping down the temperature over 1500 MCS per spin followed by 5000 - 10000 MCS per spin at the desired temperature. The resulting equilibrated configurations were used to start simulations at other fields and temperatures nearby in the phase diagram. Each temperature and field was run from two to five times with different (H,T) starting configurations. The internal energy, $<U>$, sublattice or staggered magnetization, $<M_s>$, specific heat, $<C_H>$, staggered susceptibility, $<\chi_s>$, and in plane correlation length, $<\kappa>$, were calculated using coarse-grained averaging. The uncertainties in the calculated quantities were estimated from the variations between different runs and the coarse-grained averages of each run. In order to verify that the algorithm was working correctly simulations were carried out in zero field for the case $J_c = J_{ab} = 1$. The results obtained were in good agreement with those of Kawamura (1988a, 1989) for the same size lattice.

The temperature dependence of the specific heat and staggered magnetization for zero magnetic field is shown in Figures 5.1 and 5.2 respectively. The phase transition is marked by the peak in the specific heat, which also coincides with a sharp increase in the staggered

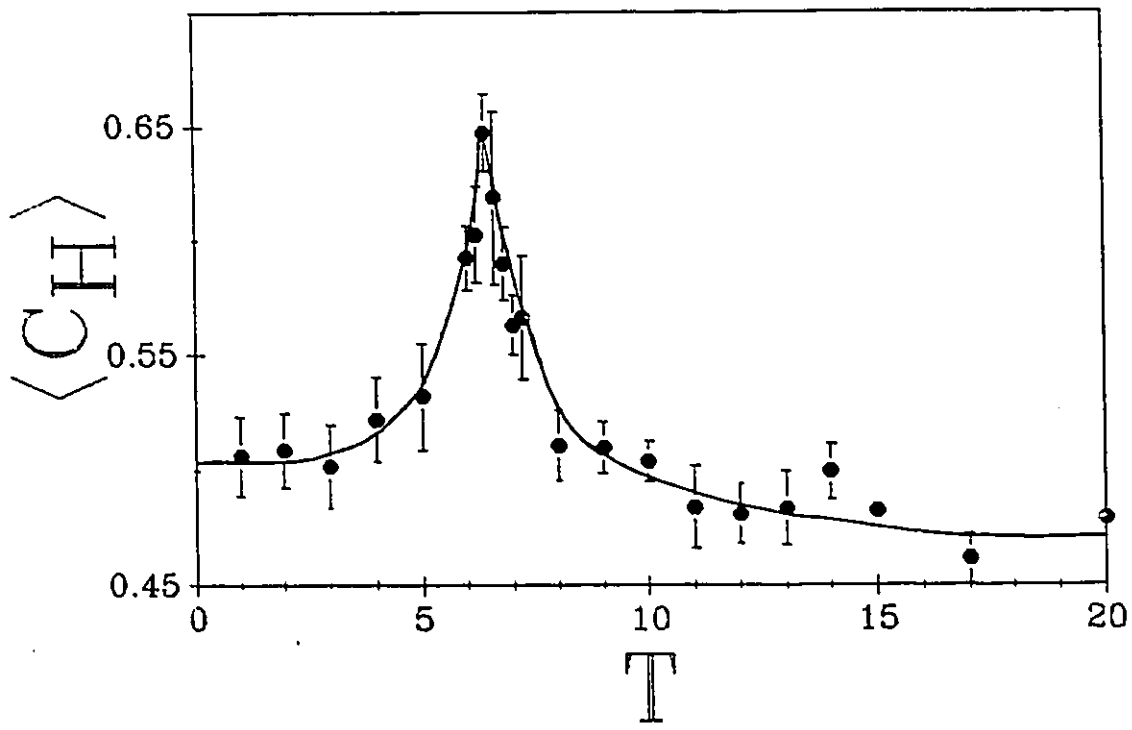

Figure 5.1: Temperature dependence of the specific heat in zero magnetic field. (dimensionless units) The line is a guide for the eye.

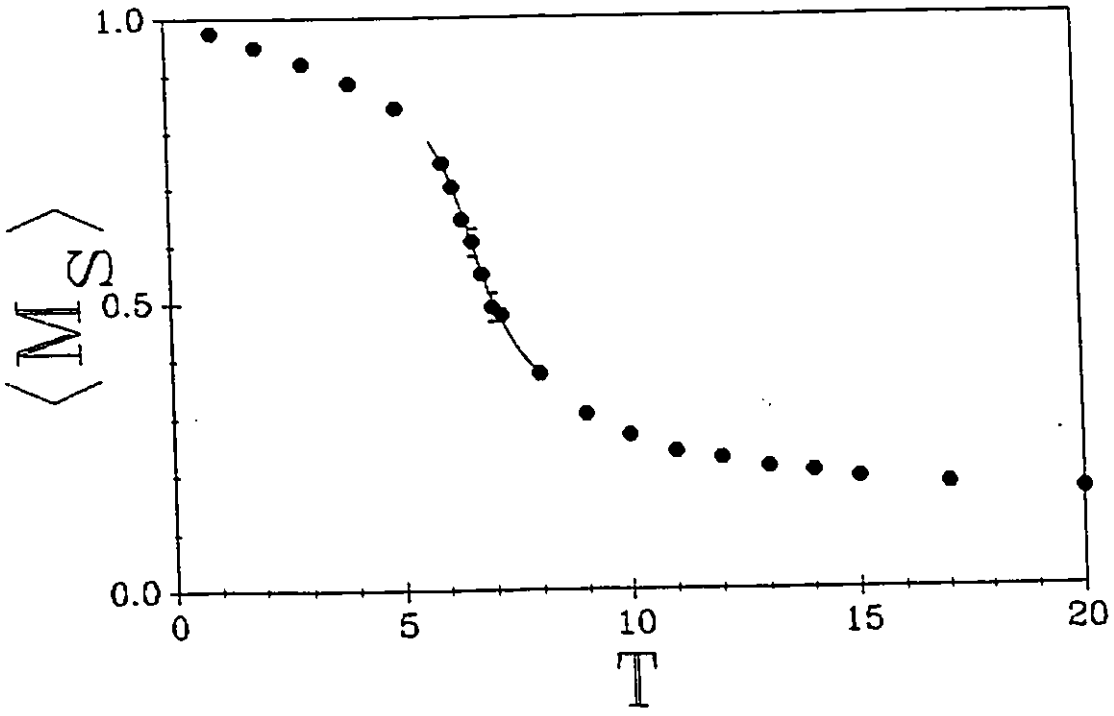

Figure 5.2: Temperature dependence of the staggered magnetization in zero field. (dimensionless units) The line is the interpolation described in the text.

magnetization. The line in Figure 5.1 is a guide to the eye. The line in Figure 5.2 is an interpolation between three long (500000 MCS per spin) simulations at dimensionless temperatures of 6.2, 6.8, and 7.4 using the configurations generated to construct a histogram of the probability distribution function which can then be transformed to nearby temperatures (Ferrenberg and Swendsen 1988). There is good agreement between the interpolation and the discrete simulations. The staggered magnetization does not go to zero above T_N due to the finite size of the lattice.

The peak in the specific heat shown in Figure 5.2 is on top of a large, almost constant, background due to the domination of the internal energy by the J_c term in the Hamiltonian. This meant that the transition temperature was better determined from the temperature dependence of the staggered susceptibility which exhibited a large peak at T_N. The temperature dependence of the staggered susceptibility in zero field and in a field of 50, in dimensionless units, is shown in Figure 5.3. The line in the zero field plot is the probability distribution function interpolation which allows a precise determination of $T_N = 6.84 \pm 0.06$. The application of a magnetic field of 50 splits the zero field transition, resulting in two peaks in the staggered susceptibility at $T_{NII} = 7.8 \pm 0.3$ and $T_{NI} = 6.0 \pm 0.2$. The dashed line in the H = 50 plot is a guide to the eye.

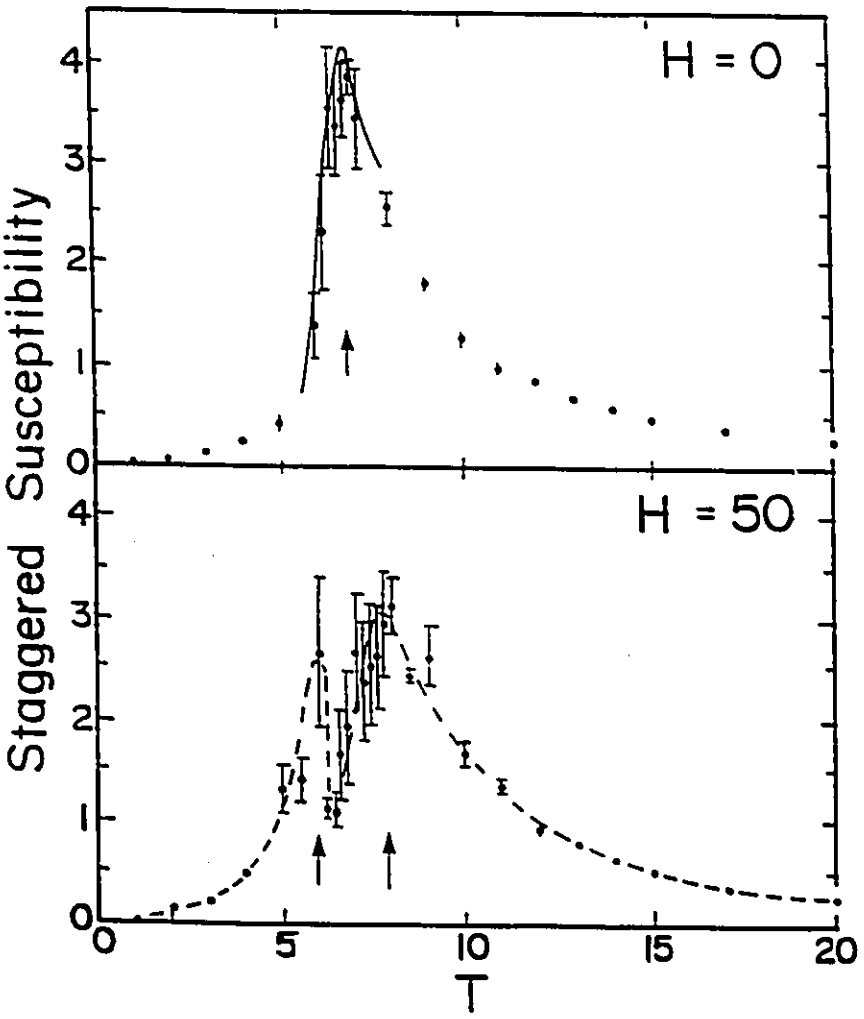

Figure 5.3: Temperature dependence of the staggered susceptibility for H = 0 and H = 50. (dimensionless units) The line in the upper plot is the interpolation described in the text. The dashed line in the lower plot is a guide to the eye; it shows the splitting of the zero field transition by the application of a magnetic field in the plane of the spins.

At low temperatures it is easier to see the phase transition by looking at the field dependence of the staggered susceptibility at constant temperature. This is shown in Figure 5.4 for T = 2. The line is a guide to the eye. There is a peak in the staggered susceptibility at H = 68 ± 2. Simulations have been carried out for temperatures between 1 and 20 and magnetic fields between 0 and 150. The location of the phase boundaries determined from the maxima in the staggered susceptibility are shown in Figure 5.5. For low values of the applied field (H < 30) the two transitions could not be separated although the increase in the width of the peak in χ_s over the H = 0 case suggests that the identificaction of the H = 0, T = T_N transition as a tetracritical point is correct. These points have been drawn half filled to reflect this. The lines in Figure 5.5 show the location of the experimentally determined phase boundaries (see Figure 4.2) with the temperature axis scaled to agree at H = 0. The zero temperature classical transition field (H = 74.4 = 6.1 T) (Chubukov 1988) is indicated by the triangle. There is good agreement between this value and the extrapolated T = 0 transition field of the simulations.

The spin structure of the two phases are shown in Figure 5.6 which is a diagram of the configuration for a region of one layer of the lattice generated at low temperature (T = 1) for magnetic fields of 20 and 90. The

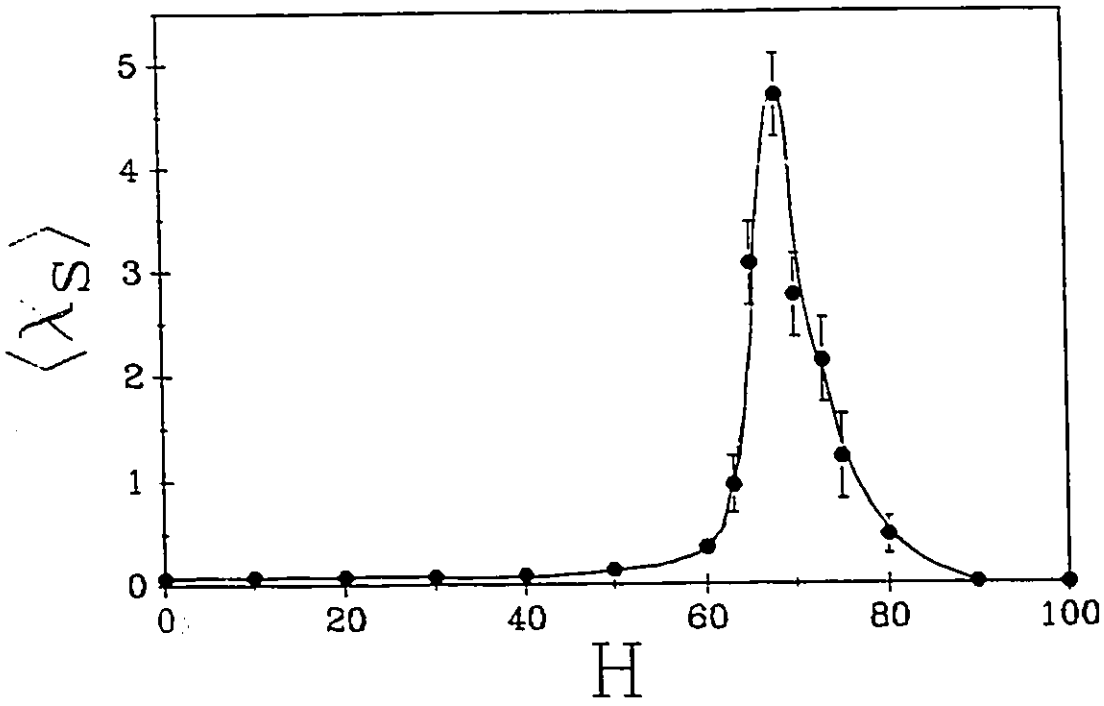

Figure 5.4: Field dependence of the staggered susceptibility for T = 2. (dimensionless units)

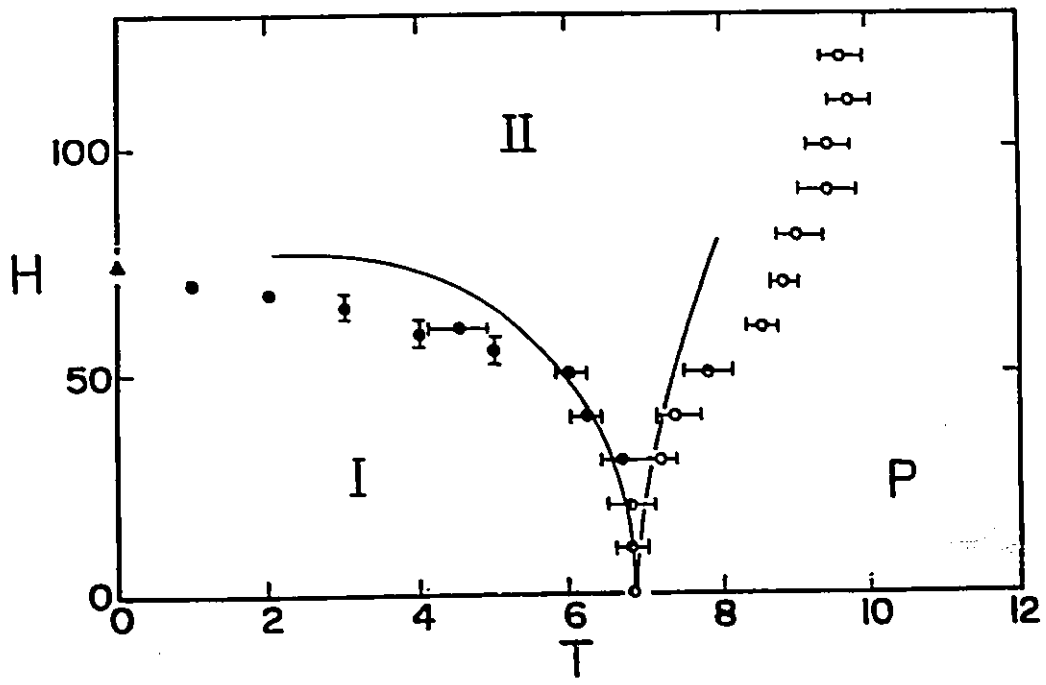

Figure 5.5: The magnetic phase diagram for the Hamiltonian (5.1). The structures of I and II are shown in Figure 5.6. P denotes the paramagnetic phase. The triangle is the classical zero temperature transition field for $CsMnBr_3$ (Chubukov 1988). The lines show the location of the experimentally determined phase boundaries scaled to agree at H = 0. (see Figure 4.2).

magnetic field is directed toward the right side of the page as indicated in the Figure. The low field phase (I) is a slight distortion of the 120° structure in which one sublattice cants toward the field from 90° while the other two sublattices collapse towards one another with increasing field. In the high field phase (II) these two sublattices collapse together and all three rotate in the field direction as the field strength increases. This is in agreement with the classical zero temperature results (Chubukov 1988) and is consistent with the measurements of chapter 4. By determining the average spin configuration over the whole simulation it was possible to verify that there was a small ferromagnetic component of the spins that increased with increasing field. This is not immediately obvious in Figure 5.6 due to the thermal fluctuations present for the instantaneous configuration shown.

5.3 Discussion

The qualitative features of the magnetic phase diagram of $CsMnBr_3$ (Figure 4.2) are well reproduced by the Monte Carlo simulations of the Hamiltonian derived from the spin wave dispersion (Gaulin et al 1987, Falk et al 1987). In particular the tetracriticality of the zero field phase transition to long range antiferromagnetic order is intrinsic to the XY model on a triangular lattice with the exchange constants appropriate for $CsMnBr_3$. The structures

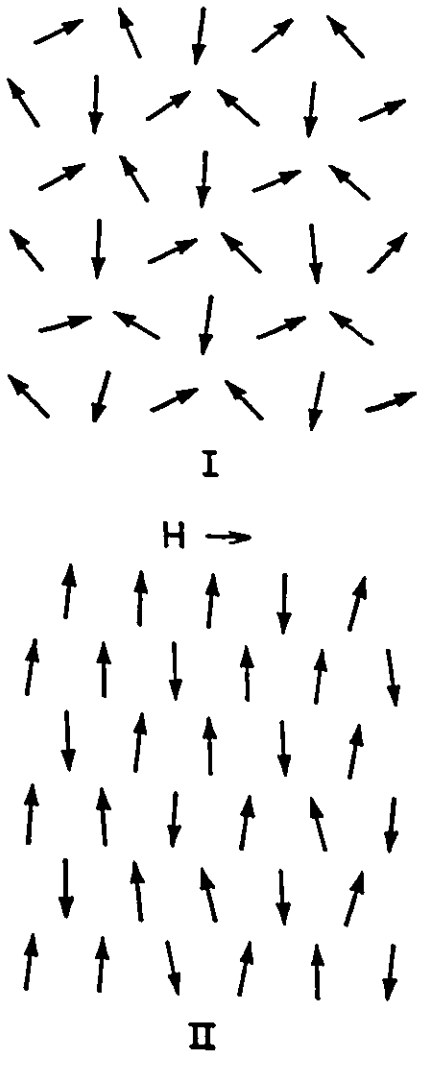

Figure 5.6: The magnetic structure for the low field (I) and high field (II) phases. The field diection is indicated in between the two spin configurations.

for the two phases are also in good agreement with the measurements. The Monte Carlo phase diagram also reproduces the increase of the upper Néel temperature (T_{NII}) with increasing magnetic field. This behaviour is not found in the mean field theory for the Hamiltonian or in Monte Carlo simulations of the XY antiferromagnet on a triangular lattice with isotropic interactions ($J_c = J_{ab}$) (Plumer 1990). The fact that the present simulations do repoduce it indicates that it is a fluctuation effect brought about by the very strong coupling between the spins along the c axis.

Although there is excellent qualitative agreement between the experimental phase diagram for $CsMnBr_3$ and the Monte Carlo simulations there is a considerable discrepancy in the values for the transition temperatures. In zero magnetic field the simulations found $T_N = 6.84 \pm 0.06$, in dimensionless units, or 1.89 K; the actual Néel temperature was 8.32 K. Simulations of $12 \times 12 \times L_c$ lattices yielded Néel temperatures of 13.1 ± 0.1 (3.6 K), 23.0 ± 0.3 (6.4 K) and 32.0 ± 0.3 (8.9 K) for $L_c = 24$, 48, and 96. This indicates that there is a substantial renormalization of T_N with the number of spins along c. The origin of this effect is the quasi-one-dimensional nature of (5.1). For shorter chain lengths the enhancement of T_N by the strong one-dimensional correlations is suppressed. This is consistent with the sharp suppression of T_N in $CsMnBr_3$ upon doping with small amounts of non-magnetic Mg (Visser et al

1988). A similar finite size scaling effect has been seen in simulations of L × L × pL lattices of quasi-one-dimensional Ising spins (Graim and Landau 1981). The size dependence of T_N for the finite lattice was found to be stronger for small p. In order to obtain the best estimate for the infinite lattice it is desirable to study the size dependence of T_N for lattices whose shape approximates that of the correlated regions of spins near T_N. The anisotropy of the correlation lengths in Figure 3.8 is about a factor of 8 so lattices of size L × L × 16L would give the best results (there are two Mn^{+2} along the c axis in one unit cell hence the factor of 16). Unfortunately, even for L = 12 this is too large a lattice to be simulated on the available hardware. The trend observed in the simulations for p = 1, 2, 4, and 8 suggests that T_N for the infinte lattice would be slightly larger than the experimental value, probably due to a reduction of the actual T_N by quantum effects (Imry et al 1975). The substantial finite size effects for these simulations also make it impossible to make reasonable estimates of the critical exponents in a magnetic field.

CHAPTER 6

CONCLUSIONS

Neutron scattering measurements of the static critical exponents γ, υ, and β for $CsMnBr_3$ have established that the phase transition that occurs in zero magnetic field at T = 8.3 K does not belong to any standard universality class (see Table III). This gives strong support to the assertion by Kawamura (1988a, 1988b, and 1989) that this material belongs to a new $Z_2 \times S_1$ universality class characterized by the symmetry of the order parameter, not just its dimensionality. This conclusion, which is also supported by the results for the Heisenberg system VCl_2 (Kadowaki et al 1987), has far reaching implications as it entails a generalization of the universality hypothesis (Kadanoff 1971).

The determination of the magnetic phase diagram of $CsMnBr_3$ has shown that this novel phase transition is a tetracritical point quite different from any previously observed. Monte Carlo simulations have shown the qualitative features of the phase diagram can be reproduced from the simple, nearest neighbour spin wave Hamiltonian without the introduction of additional terms. The tetracriticality is therefore intrinsic to the same

Hamiltonian that results in the $Z_2 \times S_1$ critical behaviour.

Although the qualitative features of the magnetic phase diagram of $CsMnBr_3$ can be understood theoretically there are discrepancies between the measured crossover exponents and the renormalization group prediction (Kawamura et al 1990). The magnetic susceptibility near the tetracritical point did not show the singularity predicted by scaling analysis (Kawamura et al 1990) although the phase transition was clearly evident as a change in the slope of χ. These two disagreements between the predicted and actual behaviour of $CsMnBr_3$ indicate that a detailed, quantitative understanding of the tetracritical point is still not available. Until these questions are resolved the status of the universality of the phase transition is uncertain.

REFERENCES

Abramowitz, M. and Stegun, I.A. (1965). *Handbook of Mathematical Functions*. p. 924. New York: Dover.

Ajiro, Y., Nakashima, T., Unno, Y., Kadowaki, H., Mekata, M., and Achiwa, N. (1988). *J. Phys. Soc. Jpn.* **57**: 2648.

Andrews, T. (1869). *Phil. Trans. R. Soc.* **159**: 575.

Baker, G.A. Jr., Nickel, B.G., and Meiron, D.I. (1978). *Phys. Rev.* **B 17**: 1365.

Belanger, D.P., Murray, W.E. Jr., and Gaulin, B.D. (1990). private communication.

Binder, K. and Heerman, D.W. (1988). *Monte Carlo Simulations in Statistical Physics*. Berlin: Springer-Verlag.

Binder, K. and Wang, J. (1989). *J. Stat. Phys.* **55**: 87.

Brockhouse, B.N. (1961). *Inelastic Scattering of Neutrons in Solids and Liquids*. p. 113. Vienna: IAEA.

Broholm, C., Lin, H., Matthews, P.T., Mason, T.E., Buyers, W.J.L., Collins, M.F., Menovsky, A.A., Mydosh, J.A., and Kjems, J.K. (1990). *Phys. Rev.* **B** to appear.

Chubukov, A.V. (1988). *J. Phys.* **C 21**: L441.

Collins, M.F. (1989). *Magnetic Critical Scattering*. Oxford: Oxford University Press.

Cooper, M.J. and Nathans, R. (1967). *Acta. Cryst.* **23**: 257.

Corliss, L.M., Hastings, J.M., Kunnmann, W., Begum, R.J., Collins, M.F., Gurewitz, E., and Mukamel, D. (1982). *Phys. Rev.* **B 25**: 245.

Cowley, R.A. (1987). *Methods of Experimental Physics*, **23 C** (K. Sköld and D.L. Price Eds.) p. 1. Orlando: Academic Press.

Eibshutz, M., Sherwood, R.C., Hsu, F.S.L., and Cox, D.E. (1973). *Magnetism and Magnetic Materials (Denver, 1972)*, Proceedings of the 18th Annual Conference on Magnetism and Magnetic Materials, AIP Conf. Proc. No. 10 (C.D. Graham Jr. and J.J. Rhyne Eds.) p.

684. New York: American Institute of Physics.

Falk, U., Furrer, A., Güdel, H.U., and Kjems, J.K. (1987). *Phys. Rev.* **B 35**: 4888.

Ferrenberg, A.M. and Swendsen, R.H. (1988). *Phys. Rev. Lett.* **23**: 2635.

Fisher, M.E. (1964). *J. Math. Phys.* **5**: 944.

Fisher, M.E. (1982). *Critical Phenomena* (F.J.W. Hahne, Ed.) Lecture Notes in Physics #186, p. 1-139. Berlin: Springer-Verlag.

Fisher, M.E. and Burford, R.J. (1967). *Phys. Rev.* **156**: 583.

Fitzgerald, W.J., Visser, D., and Ziebeck, K.R.A. (1982). *J. Phys.* **C 15**: 795.

Gaulin, B.D. (1986). *Topics in One Dimensional Magnetism.* Ph.D. Thesis, McMaster University.

Gaulin, B.D. and Collins, M.F. (1984). *Can. J. Phys.* **62**: 1132.

Gaulin, B.D., Collins, M.F., and Buyers, W.J.L. (1987). *J. Appl. Phys.* **61**: 3409.

Gaulin, B.D., Collins, M.F., and Mason, T.E. (1989a). *Physica* **B 156 & 157**: 244.7: 244.

Gaulin, B.D., Mason, T.E., Collins, M.F., and Larese, J.Z. (1989b). *Phys. Rev. Lett.* **62**: 1380.

Goodyear, J. and Kennedy, D.J. (1974). *Acta. Cryst.* **B 28**: 1640.

Graim, T. and Landau, D.P. (1981). *Phys. Rev.* **B 24**: 5156.

Griffith, R.B. (1965). *J. Chem. Phys.* **43**: 1958.

Halperin, B.I., Hohenberg, P.C., and Ma, S. (1972). *Phys. Rev. Lett.* **29**: 1548.

Halperin, B.I., Hohenberg, P.C., and Ma, S. (1974). *Phys. Rev.* **B 10**: 139.

Harrison, A. and Mason, T.E. (1990). *J. Appl. Phys.* to appear.

Imry, Y., Pincus, P., and Scalapino, D. (1975). *Phys. Rev.* **B 12**: 1978.

Kadanoff, L.P. (1966). *Physics* 2: 263.

Kadanoff, L.P. (1971). *Proc.* 1970 *Varenna Summer School on Critical Phenomena* (M.S. Green, Ed.), pp. 100-117. New York: Academic Press.

Kadowaki, H., Ubukoski, K., Hirakawa, K., Martinez, J.L., and Shirane, G. (1987). *J. Phys. Soc. Jpn.* **56**: 1294.

Kadowaki, H., Shapiro, S.M., Inami, T., and Ajiro, Y. (1988). *J. Phys. Soc. Jpn.* **57**: 2460.

Kawamura, H. (1988a). *J. Appl. Phys.* **63**: 6086.

Kawamura, H. (1988b). *Phys. Rev.* **B 38**: 4916.

Kawamura, H. (1989). *J. Phys. Soc. Jpn.* **58**: 584.

Kawamura, H., Caillé, A., and Plumer, M.L. (1990). *Phys. Rev.* **B 41**: 4416.

Kerszberg, M. and Mukamel, D. (1978). *Phys. Rev.* **B 18**: 6283.

Loopstra, B.O. (1966). *Nucl. Instrum. Meth.* **44**: 181.

Lovesey, S.W. (1984). *Theory of Neutron Scattering from Condensed Matter*. Oxford: Oxford University Press.

Mason, T.E., Collins, M.F., and Gaulin, B.D. (1987). *J. Phys.* **C 20**: L945.

Mason, T.E., Gaulin, B.D., and Collins, M.F. (1989). *Phys. Rev.* **B 39**: 586.

Mason, T.E., Stager, C.V., Gaulin, B.D., and Collins, M.F. (1990a). *Phys. Rev.* **B** to appear.

Mason, T.E., Collins, M.F., and Gaulin, B.D. (1990b). *J. Appl. Phys.* to appear.

Mason, T.E., Lin, H., Collins, M.F., Buyers, W.J.L., Menovsky, A.A., and Mydosh, J.A. (1990c). *Physica* **B** to appear.

Metropolis, N., Rosenbluth, A.W., Rosenbluth, M.N., Teller, A.H., and Teller, E. (1953). *J. Chem. Phys.* **21**: 1087.

Muller, K.A., Berlinger, W., Drumheller, J.E., and Bednorz, J.G. (1983). *Multicritical Phenomena* (R. Pynn and A. Skjeltorp Eds.) p. 143. New York: Plenum.

Niedermayer, F. (1988). *Phys. Rev. Lett.* **61**: 2026.

Nielsen, M. and Möller, H.B. (1969). *Acta. Cryst.* **A25**: 567.

Ornstein, L.S. and Zernicke, F. (1914). *Proc. Sect. Sci. K. Med. Akad. Wet.* **17**: 793.

Plumer, M.L., Caillé, A., and Hood, K. (1989). *Phys. Rev.* **B 39**: 4489.

Plumer, M.L., and Caillé, A. (1990). *Phys. Rev.* **B 41**: 2543.

Plumer, M.L. (1990). private communication.

Press, W.H., Flannery, B.P., Teukolsky, S.A., and Vetterling, W.T. (1986). *Numerical Recipes*. Cambridge: Cambridge University Press.

Rohrer, H. and Gerber, Ch. (1977). *Phys. Rev. Lett.* **38**: 909.

Rushbrooke, G.S. (1963). *J. Chem. Phys.* **39**: 842.

Shapira, Y. and Foner, S. (1970). *Phys. Rev.* **B 1**: 3083.

Shirane, G. and Minkiewicz, V.J. (1970). *Nucl. Instrum. Meth.* **89**: 109.

Squires, G.L. (1978). *Introduction to the Theory of Thermal Neutron Scattering*. Cambridge: Cambridge University Press.

Stanley, H.E. (1971). *Introduction to Phase Transitions and Critical Phenomena*. Oxford: Oxford University Press.

Steeman, R.A., Mason, T.E., Lin, H., Buyers, W.J.L., Menovsky, A.A., Collins, M.F., Frikkee, E., Nieuwenhuys, G.J., and Mydosh, J.A. (1990). *J. Appl. Phys.* to appear.

Steinitz, M.O., Kahrizi, M., and Tindall, D.A. (1987). *Phys. Rev.* **B 36**: 783.

Tranquada, J.M., Buyers, W.J.L., Chou, H., Mason, T.E., Sato, M., Shamoto, S., and Shirane, G. (1990). *Phys. Rev. Lett.* **64**: 800.

Tucciarone, A., Lau, H.Y., Corliss, L.M., Delapalme, A., and Hastings, J.M. (1971). *Phys. Rev.* **B 4**: 3206.

Visser, D., Harrison, A., and McIntyre, G.J. (1988). *J. de Phys.* **C8**: 1255.

Watson, R.E. and Freeman, A.J. (1961). *Acta. Cryst.* **14**: 27.

Wilson, K.G. and Kogut, J. (1974). *Phys. Rep.* **12**: 75.